

https://dspace.org/

Modelling OAM Crosstalk with Neural Networks: Impact of Tip/tilt and Lateral Displacement

Makoni, Steven Gamuchirai

2024
University of the Witwatersrand, Johannesburg
https://hdl.handle.net/10539/45428
Makoni, Steven Gamuchirai. (2024). Modelling OAM Crosstalk with Neural Networks: Impact of Tip/tilt and Lateral Displacement [Masters dissertation, University of the Witwatersrand, Johannesburg]. WIReDSpace.

Downloaded from a DSpace repository. https://dspace.org/



UNIVERSITY OF THE
WITWATERSRAND,
JOHANNESBURG

Modelling OAM Crosstalk with Neural Networks: Impact of Tip/tilt and Lateral Displacement

Steven Gamuchirai Makoni

Supervisors: Dr. Mitchell Cox and Prof. Ling Cheng

A dissertation submitted to the Faculty of Engineering and the Built Environment, University of the Witwatersrand, Johannesburg, in fulfilment of the requirements for the degree of
Master of Science in Engineering.

2024

Declaration

I, the undersigned, hereby declare that the work contained in this dissertation is my own original work and that I have not previously in its entirety or in part submitted it at any university for a degree.



Steven Gamuchirai Makoni

Braamfontein, Johannesburg
August 8, 2024

Abstract

This research focuses on a critical challenge within Free Space Optical (FSO) communication systems, specifically those utilizing Mode Division Multiplexing (MDM) with Orbital Angular Momentum (OAM) modes of a limited transmission range. Despite these systems' potential to significantly enhance spectral efficiency and transmission capacity, their effectiveness is hindered by the limited range caused by atmospheric turbulence-induced aberrations. Atmospheric turbulence and misalignments distort the optical wavefront, causing degradation in orthogonal spatial modes and resulting in power spreading into adjacent modes, known as crosstalk in MDM systems.

This research presents a simple neural network model for estimating OAM crosstalk in FSO systems, specifically focusing on atmospheric turbulence-induced aberrations. Firstly, we generated datasets through simulation and experimentation for validation purposes. We then develop and evaluate the neural network model, assessing its accuracy under various turbulence aberrations. The simple neural network, trained solely on tip/tilt and displacement inputs and without retraining, accurately estimated OAM spectra using approximated inputs in turbulent conditions, closely matching experimentally measured spectra. Despite the presence of turbulent aberrations, the model showed a minimal decrease in the coefficient of determination, indicating its ability to generalize well to unseen measurements.

Our findings indicate that a simple neural network trained solely on tilt and displacement inputs can accurately estimate OAM crosstalk amidst many turbulence aberrations for $\ell \in$ [-5, 5] as a proof of concept. This implies that simple detectors such as cameras can be used to implement or optimize digital signal processing for error detection and correction utilizing the knowledge of crosstalk, offering promising avenues for improving system efficiency and quality of service for MDM systems.

In summary, this research leveraged neural networks to model OAM crosstalk induced by misalignments and turbulence. The model's ability to estimate OAM crosstalk due to misalignments and atmospheric turbulence shows potential for use in real-time predictive systems. With further refinement, neural network models could indicate the evolution of OAM crosstalk in FSO communications that employ OAM multiplexing schemes in atmospheric turbulence. The demonstrated efficacy of the neural network model positions it as a valuable tool for enhancing the robustness of FSO communications employing higher-order OAM modes.

Acknowledgements

I am deeply grateful to my supervisors, Dr. Mitchell Cox and Prof. Ling Cheng, for their invaluable guidance, support, and expertise throughout the entire process of this project. I am grateful for all the discussions we have had and the tips (both small and large) on how to perform excellent scientific research.

I owe my family and friends an immense debt of gratitude. Their prayers, unwavering moral support, flexibility, and understanding during the late nights of work or when I had to disappear have been my pillars of strength. I could not have reached this milestone without you by my side.

A heartfelt thank you goes to my dedicated research team, the Wits Optical Communication Lab group: Fortune Iga (who was writing his dissertation at the same time as me), Alice Drodzov (she held my hand during the early days of my research), Elijah Kadimba (we came a long way together), Mikaeel Dindar, and Christopher Rawlings. Their technical expertise, moral support, and daily funny conversations during my master's studies have made this journey memorable and enjoyable.

I want to thank the Center for Telecommunications Access and Services (CeTAS) for their generous financial support over the past two years. This support has allowed me to pursue my studies and provided for my upkeep. Additionally, I am thankful to the School of Electrical and Information Engineering (EIE) for the Teaching Assistant job, which enriched my academic experience and provided valuable insights into the field.

Contents

Declaration i

Abstract ii

Acknowledgements iii

List of Figures vi

List of Tables x

List of Acronyms xi

Resulting Publications xiii

1 Introduction 1
- 1.1 Demonstrations of MDM FSO Links . . . 2
- 1.2 Problem Statement . . . 3
- 1.3 Problem Objective and Scope . . . 4

2 Background 5
- 2.1 Spatial Modes of Light . . . 5
  - 2.1.1 Gaussian Mode . . . 6
  - 2.1.2 Laguerre-Gaussian Modes . . . 6
  - 2.1.3 Mode Characterization by Modal Decomposition . . . 7
- 2.2 Atmospheric Turbulence . . . 9
  - 2.2.1 Kolmogorov Model . . . 9
  - 2.2.2 Beam Wander . . . 9
  - 2.2.3 Beam Spreading . . . 10
  - 2.2.4 Scintilation . . . 10
- 2.3 OAM Modal Crosstalk Models . . . 11
  - 2.3.1 Tip/Tilt and Displacement . . . 11
  - 2.3.2 Turbulence Induced . . . 12
- 2.4 Deep Neural Networks . . . 13
  - 2.4.1 Architecture . . . 13
  - 2.4.2 Activation Functions . . . 14
  - 2.4.3 Training Process . . . 14

3 OAM Crosstalk Measurements Validation: Experiment vs. Simulation 17
- 3.1 Experimental Setup and Methodology . . . 18

3.2 Displacement and Tip/Tilt Dataset . . . 18
3.3 Validation of Dataset . . . 21
3.3.1 Comparison of Measured and Simulated OAM Spectra . . . 21
3.3.2 Verification of Lateral Displacement and Tip/Tilt . . . 25
3.4 Summary . . . 26

4 A Neural Network Model for OAM Crosstalk with Tilt and Displacement 27
4.1 Model Development and Methodology . . . 27
4.2 Architecture . . . 28
4.2.1 Input and Output Pre-processing . . . 28
4.2.2 Input Layer . . . 29
4.2.3 Hidden Layer Layer . . . 29
4.2.4 Output Layer . . . 29
4.3 Training Process . . . 30
4.4 Performance Metrics . . . 31
4.5 Results and Discussion . . . 32
4.5.1 Correlation of the Model on the 3 Cases . . . 32
4.5.2 Correlation of the Output Neurons . . . 32
4.5.3 Measured, Simulated and NN-estimated Spectra . . . 34
4.5.4 Hyperparameters optimisation . . . 37
4.6 Conclusion . . . 38

5 Accuracy of the Simplified Model in Turbulence 40
5.1 Experimental Setup and Methodology . . . 41
5.1.1 Simulating Turbulence with Zernike polynomials . . . 42
5.1.2 Experimental Verification of the Phase Screens . . . 43
5.1.3 Approximation of Tip/Tilt Zernike Terms . . . 44
5.2 Results and Discussion . . . 46
5.2.1 Comparison of NN-estimation with Measured Turbulent OAM Spectra . . . 46
5.3 Conclusion . . . 47

6 Conclusion 50
6.1 Future Work . . . 51

References 52

List of Figures

2.1 Intensity patterns with inset phase of Laguerre-Gaussian (only OAM modes indicated where $p = 0$). 7

2.2 Illustration of lateral displacement and tip/tilt angle. The beam axis is the axis on which the beam propagates. The measurement axis is the axis at which the intensity of the beam is measured at the detector spot. Lateral displacement, Δy, is the offset of the beam axis vertically (or horizontally) parallel to the measurement axis. Tip/Tilt, α, is when the beam axis is at an angle upon beam arrival at the detector spot. Therefore, lateral displacement and tip/tilt cause the beam axis to be misaligned with the measurement axis. 12

2.3 Architecture of a feedforward neural network structure showing the inputs, hidden and output layers. The neural network learning process is shown, illustrating the forward propagation of inputs through hidden layers to output, backward propagation of error, weight optimisation, and loss calculation with model estimations and true values. 13

3.1 The experimental setup used in this work is equivalent to the simulation setup used to perform a modal decomposition. The beam splitters, BS1 and BS2, direct the beam to the SLM for modal decomposition and to the two cameras to measure the tip/tilt and displacement values. Cameras 1 and 2 are used for displacement and tip/tilt measurements. 19

3.2 Experiment schematic of how the SLM is used to impose both lateral displacement and tip/tilt angle on the first SLM hologram. During mode creation, the SLM-imposed lateral displacements and tip/tilt are achieved by specifying values of Δx, Δy, β α. Displacement was measured using the camera at the 4f point, position 1. The camera at the 2f point measured the offset caused by tip/tilt that is used to calculate tip/tilt. 20

3.3 Measurement of OAM crosstalk ($\ell_{\text{input}} = 0$) with increasing displacement for the displacement-only case. 22

3.4 Measurement of OAM crosstalk ($\ell_{\text{input}} = 0$) with increasing tip/tilt for the tip/tilt only case. 22

3.5 Measurement of OAM crosstalk ($\ell_{\text{input}} = 0$) with increasing tip/tilt and/or displacement for the case of a combination of both. OAM crosstalk measurement is shown when tip/tilt and displacement values imposed are considered separately. 23

3.6 Correlation plots of simulated and (experimentally) measured normalised power with (a) tilt only, (b) lateral displacement only, and (c) a combination of both. High correlation coefficients: (a) 0.96, (b) 0.96, (c) 0.93, showing strong agreement in all cases. 23
3.7 Residual plots showing three different cases with (a) tilt only, (b) lateral displacement only, and (c) a combination of both. The histogram of the residuals exhibits a random Gaussian characteristic shape. The RMSE value is slightly higher in the case of a combination of both. 23
3.8 Model accuracy only shows several cases with lateral displacement. Blue bars are the ground truth modal decomposition; red bars are the simulated decomposition that will be used to train the Neural Network (NN). The input modes shown are ℓ_{input} = -3, 0 and 3 in the top, middle, and bottom rows, respectively, with increasing displacement magnitude. 24
3.9 Model accuracy shows only several cases with tip/tilt. Blue bars are the ground truth modal decomposition; red bars are the simulated decomposition that will be used to train the NN. The input modes shown are ℓ_{input} = -3, 0 and 3 in the top, middle, and bottom rows, respectively, with increasing tip/tilt magnitude. 24
3.10 Model accuracy shows several cases with lateral displacement and tip/tilt. Blue bars are the ground truth modal decomposition; red bars are the simulated decomposition that will be used to train the NN. The input modes shown are ℓ_{input} = -3, 0 and 3 in the top, middle, and bottom rows, respectively, with increasing misalignment magnitude. 24
3.11 Plots showing the experimentally verified measurements of tip/tilt and lateral displacement in orange and green - the discrepancy is due to slight misalignments in the setup. 25

4.1 A methodology overview of the OAM crosstalk modelling using a simple neural network. The illustration shows the neural network development process and how it is linked to Chapter 3 and Chapter 5. 28
4.2 Architecture of the neural network structure with dimensions of 15 inputs and 11 outputs. The input nodes consists of displacement and tip/tilt and representation of $\ell_{\text{input}} \in$ [-5, 5]. The output nodes represent the normalised in the basis modes adjacent to the input mode, ℓ_{input} i.e OAM spectra. 30
4.3 Correlation and residual histogram of normalised power for $\ell_{\text{input}} \in [-5, 5]$ between simulated and NN-estimated values when there is only displacement only. The correlation plot illustrates the relationship between the simulated and NN-estimated values, with a correlation of determination values of R^2 = 99.29%, indicating a strong match. The residual histogram displays a Gaussian distribution of errors, showing the model's accuracy and good estimation of training and validation datasets. 33

4.4 Correlation and residual histogram of normalised power for $\ell_{\text{input}} \in [-5, 5]$ between simulated and NN-estimated values when there is only tip/tilt only. The correlation plot illustrates the relationship between the simulated and NN-estimated values, with a correlation of determination values of R^2 = 99.82%, indicating a strong match. The residual histogram displays a Gaussian distribution of errors, showing the model's accuracy and good estimation of training and validation datasets. The training and validation datasets were split with a ratio of 70:30. 33
4.5 Correlation and residual histogram of normalised power for $\ell_{\text{input}} \in [-5, 5]$ between simulated and NN-estimated values for the case of the combination of tip/tilt and displacement. The correlation plot illustrates the relationship between the simulated and NN-estimated values, with a correlation of determination values of R^2 = 99.72%, indicating a strong match. The residual histogram displays a Gaussian distribution of errors, showing the model's accuracy and good estimation of training and validation datasets. 34
4.6 Correlation analysis across 11 output nodes denoted by $\Delta\ell$. The subfigures show how the model's estimation matches actual values for different output neurons. Neuron $\Delta\ell$ = 0 corresponds to the input mode, while adjacent neurons represent neighbouring modes (crosstalk). The green and red dots denote training and validation normalised power values. The subplots showcase average RMSE and R^2 values on the training and validation dataset. 35
4.7 Model accuracy is illustrated across the case with lateral displacement only. Blue bars: Experimentally measured normalised power values (Ground Truth); Red bars: Simulated normalised power (used for NN training); Orange bars: NN-estimated with the final model. Input modes: ℓ_{input} = -3, 0, and 3 in the top, middle, and bottom rows, respectively, with increasing displacement magnitude from Figure 4.7a to 4.7c. 36
4.8 Model accuracy is illustrated across the case with tip/tilt only. Blue bars: Experimentally measured normalised power values (Ground Truth); Red bars: Simulated normalised power (used for NN training); Orange bars: NN-estimated with the final model. Input modes: ℓ_{input} = -3, 0, and 3 in the top, middle, and bottom rows, respectively, with increasing tip/tilt magnitude from Figure 4.8a to 4.8c. 36
4.9 Model accuracy is illustrated across the case with lateral displacement and tip/tilt combined. Blue bars: Experimentally measured normalised power values (Ground Truth); Red bars: Simulated normalised power (used for NN training); Orange bars: NN-estimated with the final model. Input modes: ℓ_{input} = -3, 0, and 3 in the top, middle, and bottom rows, respectively, with increasing misalignment magnitude from Figure 4.9a to 4.9c. 36
4.10 Comparing training and validation losses for different scenarios. 37
4.11 Training and validation losses for different neurons in 1 hidden layer. The average MSE loss is shown for an increasing number of neurons. . . 38
4.12 Training and validation losses for neurons in 2 hidden layers. The average MSE loss is shown for an increasing number of neurons. 38

4.13 Training and validation losses for different neurons in 3 hidden layers. The average MSE loss is shown for an increasing number of neurons. . . 38

5.1 The setup simulates turbulence using Zernike polynomials. 41
5.2 The Strehl ratio for a set of experimentally generated phase screens using the Zernike (Noll) methods. Theoretical values are plotted as solid lines, and experimentally measured points are represented as red dots superimposed with standard error bars. Experimental measurements of the Strehl Ratio show a close match to the theory. 44
5.3 Experimental validation of Zernike tip/tilt terms, illustrated by (a) the presence (green dots) and absence (red dots) of higher-order Zernike terms under turbulence strengths, $D/r_0 = 1$ and 3. (b) Random images of the Gaussian beam under turbulence strengths, $D/r_0 = 1$ and 3, demonstrating the evolving profile and distribution with the introduction of tip/tilt terms alone and in combination with higher-order terms. . . . 46
5.4 In the presence of turbulence, we can still estimate the tip/tilt and displacement. The approximated tip/tilt and displacement values and their corresponding OAM spectra of random input modes, $\ell_{\text{input}} \in$ [-5,5], were used to generate the unseen dataset to test the NN model without retraining the model. The bar plots above show the NN-estimated OAM spectra without retraining (in green) and measured spectra due to simulated turbulence (in red). The RMSE between the two spectra is shown in each plot. 47
5.5 The correlation plot shows a comparison between NN-estimated OAM spectra and experimentally measured spectra for the measurements approximated in the presence of turbulence (in green) and the known tip/tilt and displacement measured in Chapter 3 (in red). The coefficient of determination for the measurements with tip/tilt and displacement (in green) and in the presence of turbulence (in red). 48
5.6 Residual plots showing the average RMSE for the measurements with tip/tilt and displacement (in green) and in the presence of turbulence (in red). The histogram of the residuals exhibits a random Gaussian characteristic shape. 49

List of Tables

5.1 A few selected Zernike polynomials terms mapped to well-known wavefront aberrations. 43

List of Acronyms

AO	Adaptive Optics
BS	Beam Splitter
CNN	Convolutional Neural Network
DNN	Deep Neural Network
DMD	Digital Micromirror Device
DSP	Digital Signal Processing
EM	Electromagnetic
FFNN	Feedforward Neural Network
FSO	Free Space Optical
Gbps	Gigabits per second
HG	Hermite–Gaussian
LG	Laguerre-Gaussian
MDM	Mode Division Multiplexing
MIMO	Multiple Input Multiple Output
MAE	Mean Absolute Error
MSE	Mean Square Error
NN	Neural Network
OAM	Orbital Angular Momentum
Pbps	Petabits per second
PDM	Polarization Division Multiplexing
RF	Radio Frequency
ReLU	Rectified Linear Unit
RMSE	Root Mean Square Error

RNN Recurrent Neural Network

SDM Space Division Multiplexing

SLM Spatial Light Modulator

SR Strehl Ratio

WDM Wavelength Division Multiplexing

Resulting Publications

Conference Proceedings

1. Steven G. Makoni, Ling Cheng and Mitchell A. Cox, "Investigating the effects of turbulence-induced tilt and lateral displacement on OAM modes," in The Proceedings of SAIP2022, the 66th Annual Conference of the South African Institute of Physics, edited by Prof. Aletta Prinsloo, (UJ), pp. 547 - 552. ISBN: 978-0-6397-4426-1. Available online at `http://events.saip.org.za`

CHAPTER 1

Introduction

FREE-SPACE Optical communication links are essential in many data transfer applications, and they can use either optical or Radio Frequency (RF) waves [1–3]. However, with the increasing demand for data, there is a keen interest in enhancing the data capacity of such communication systems. Multiplexing techniques have been utilised in optical communication systems to achieve this. Multiple independent data channels can be multiplexed and transmitted at the same time. This can be achieved by using various Electromagnetic (EM) wave properties, such as time, wavelength, and polarization [4]. Multiple data streams can be efficiently multiplexed and demultiplexed using appropriate device technologies. It could be necessary to use new forms of data channel multiplexing to meet future bandwidth needs [5–7].

A technique used in optical communication called Space Division Multiplexing (SDM), which allows multiple data streams to be transmitted simultaneously through the use of the spatial property of an EM wave, has gained interest recently [6]. Mode-division multiplexing is an example of SDM that uses orthogonal spatially overlapping and co-propagating spatial modes [5]. Multiple independent channels are transmitted simultaneously via multiple beams in an orthogonal spatial mode at the transmitter. This enables the receiver to separate and identify each channel. With an Mode Division Multiplexing (MDM) system, N orthogonal beams can be transmitted simultaneously, each carrying an M-bit/s data channel. This results in an aggregate transmitted data rate of $N \times M$ bit/s [8]. Therefore, the system's spectral efficiency (bits per second per hertz) and transmission capacity can be increased by a factor equal to the number of transmitted spatial modes [9, 10].

In 1992, Allen et al. [11] first reported that an optical vortex beam could carry Orbital Angular Momentum (OAM). Their work paved the way for utilising OAM, which is a subset of Laguerre-Gaussian (LG) modes, as an orthogonal spatial modal basis set for SDM [11, 12]. Beams carrying OAM (i) have a transverse phase of the form and are proportional to $e^{i\ell\phi}$ that "twists" in a helical form as it propagates, where ϕ is the azimuthal angle and ℓ is the OAM charge, (ii) can be characterised by the OAM charge $\pm\ell$ which is an unbounded integer that represents the number of 2π phase changes in the azimuthal direction [13]. The wavefront of an OAM beam twists along the propagation direction, and the twisting rate depends on the beam's OAM charge, ℓ [14]. This results in a ring-shaped intensity profile with a central null—a line of undefined phase and zero intensity along the optical path. Beams carrying with different charges, ℓ are mutually orthogonal [14], which means they act as independent channel carriers for efficiently multiplexing and demultiplexing multiple information-bearing signals [13]. OAM multiplexing can be used with other

existing multiplexing techniques, such as Wavelength Division Multiplexing (WDM) and Polarization Division Multiplexing (PDM). This is because OAM is an EM wave property independent of other properties such as wavelength and polarization. Beams with the same wavelength and polarization can be reused by applying different OAM charges to each of the many beams. This enables a potentially significant increase in the system transmission capacity [15, 16].

However, FSO links are susceptible to various random time-varying channel conditions that can distort the transmitted beam, causing significant power loss, system performance degradation and even link outages [17, 18]. These various channel conditions, such as weather or atmospheric turbulence, exhibit significant dynamic variations in amplitude as they change over time. Some approaches have been used to minimise most of the effects of the channel conditions, such as using specific wavelengths that are robust in different weather conditions [19, 20]. Atmospheric turbulence is a major limiting factor that leads to random variations in the refractive index along the transmission path, ultimately distorting the helical phase front of beams carrying OAM [19]. The effects of atmospheric turbulence on the helical phase front of OAM beams become more challenging because the proper demultiplexing of the received OAM beams depends on their helical phase-front structures [21, 22]. This may lead to fluctuations in the power of received OAM channels and inter-modal crosstalk between channels with different values, which are of significant importance in FSO, with crosstalk being of particular concern due to its ease of occurrence [23]. Understanding this crosstalk is the emphasis of this work.

1.1 Demonstrations of MDM FSO Links

There have been numerous demonstrations of MDM, some of which are impressive but held back by crosstalk. MDM systems have been successfully demonstrated across both laboratory and outdoor settings [7, 15, 16, 24–26]. These systems have also been helpful in underwater water communication [27] and communications between moving platforms, such as ground-to-unmanned aerial vehicles [28]. In MDM Free Space Optical (FSO) systems, using the orthogonality between modes often involves adjusting one-dimensional modal indices. Also, the expansion to two-dimensional mode indices, e.g. using LG, opens up a larger two-dimensional modal space, facilitating the multiplexing of additional data channels for MDM systems [29, 30]. We will focus only on the demonstration of MDM with varying one-dimensional mode indices, i.e. MDM that uses OAM modes with varied ℓ OAM charge.

Using OAM modes for FSO systems was initially introduced and demonstrated by Gibson et al. in 2004 [6]. OAM modes were transmitted over a distance of 142km in free space conditions with good mode quality. However, no information about the data rate was provided, and a neural network was used at the receiver to detect the mode with an accuracy of 82% [31]. Their work showcased the excellent results of OAM modes critical shifting, where the information is encoded in the value ℓ of the OAM beam. Subsequent research revealed that each beam could serve as a transmission medium, and a set of orthogonal OAM beams could be utilised to spatially multiplex numerous data streams [16, 29, 32]. The first MDM demonstrations were conducted in the lab, which involved sending two multiplexed beams, each carrying an on-off keying signal [32, 33]. The following experiments demonstrate the ability to multiplex and transmit an expanded set of OAM modes. In 2011, Wang et al. [34] first reported a terabit per second free-space link using four OAM modes for OAM multiplexing combined with polarization multiplexing over lab environments. Notable demonstrations of OAM multiplexing are usually done with a combination of other forms of multiplexing achieving transmission rates above 100Tbps in lab environments [7, 15, 16, 35] and in addition to these lab-scale high-rate data experiments, above 400 Gigabits per second (Gbps) transmission rates were achieved for distances under 1 km in free space [24–26, 36, 37] Both use less than 50 OAM modes maximum. The highest-

speed MDM demonstration achieved a transmission rate of 1.036 Petabits per second (Pbps) in a lab environment, employing 26 OAM modes in conjunction with wavelength and polarization [16, 37]. In turbulent conditions, the farthest MDM FSO communication test achieved 80 Gbps over about 260 meters [37, 38]. These differences in transmission rates and distances of FSO links between the lab and the outdoor demonstrations show the significant challenge posed by turbulence in OAM beams within MDM systems. Given that published outdoor demonstrations of single-Gaussian beam FSO links can span tens of kilometres [39]. In contrast, demonstrations of MDM FSO links are typically limited to relatively shorter distances (e.g., less than several hundred meters) [25, 26, 36]. These effects are mostly (i) the beam divergence observed in higher-order beams and (ii) the occurrence of OAM crosstalk, which arises from different link impairments like turbulence and link misalignment. Atmospheric turbulence induces aberrations in the optical wavefront, leading to the degradation of orthogonal spatial modes in MDM systems, which results in the spreading of power into neighbouring modes - crosstalk.

1.2 Problem Statement

From the previous section, it is clear that MDM has been demonstrated to transfer information over a few hundred meters with insignificant errors showing increasing bandwidth in FSO. However, a few meters is not long enough, especially to solve the last-mile problem. The challenge comes now when an attempt is made to extend the range of FSO-MDM over kilometres due to atmospheric turbulence because, in the kilometre range, the strength of turbulence becomes severe and causes excessive crosstalk, which inherently degrades the system's performance. The receiver size and the rapid beam expansion with increasing mode order and communication distance severely limit the practically addressable number of spatial sub-channels. Reliable and high-speed long-distance MDM systems are highly challenging because of crosstalk issues. Therefore, there is a need for more research on increasing the distance of free-space optical communication links, particularly MDM systems where OAM beams are affected by atmospheric turbulence causing crosstalk, and there is increased turbulence strength. A few works have been done to improve their range, which is critical to their versatility. This work is focused on understanding the fundamentals of OAM crosstalk due to turbulence without mitigation OAM crosstalk. This research aims to develop a neural network model for OAM crosstalk caused by the effects of atmospheric turbulence. To do that, the broad research question is:

How can neural networks be used to model OAM crosstalk in FSO systems using OAM modes, particularly in the presence of atmospheric turbulence-induced aberrations such as lateral displacement, tip/tilt, and other aberrations?

To limit the scope, the broad research question is divided into three sub-research questions:

1. There is a correlation between lateral displacement and tip/tilt on an incoming wavefront, and OAM crosstalk has been modelled analytically for Gaussian mode only [40]. When an OAM beam experiences lateral displacement or tip/tilt individually, the resulting OAM spectrum remains symmetric around the input mode, preserving the total OAM despite the misalignments. The OAM power spectrum for a displaced or tilted mode shows increased broadening with an increase in the magnitude of displacement or tilt [41]. Similarly, the OAM spectrum of a deflected Gaussian beam possesses a symmetric nature: *In light of these characteristics, how does a simple neural network perform in estimating OAM crosstalk under displacement-only and tilt-only misalignments?*

2. In practical scenarios, a light beam may experience tip/tilt and displacement. The transformation of an OAM mode under simultaneous displacement and tilt results in an OAM spectrum that is no longer symmetric except for specific combinations.

The total OAM projection becomes a superposition of intrinsic and extrinsic OAM, where the extrinsic OAM depends on both the displacement and tilt angles. This combination of displacement and tilt complicates the OAM spectrum, leading to variations in the OAM spectrum that are also dependent on the beam's orientation [41]. *In the scenario of combined displacement and tilt misalignments, is the impact noticeable on the neural network's ability to estimate OAM crosstalk?*

3. Among the various effects caused by turbulence, two fundamental ones are lateral displacement and fluctuations in the angle of arrival, also known as tip/tilt [42, 43]. These effects result in random movement of the beam at the receiver, leading to errors in OAM crosstalk. Tip/tilt terms play a substantial role in atmospheric turbulence, often accounting for 86% of the mean-square phase value compared to other aberrations [18, 42]. The simple neural network model from the previous questions was based on $\approx 86\%$ of the effects of turbulence, specifically lateral displacement and tilt. However, turbulence encompasses a broader range of effects beyond displacement and tilt. The remaining $\approx 14\%$ of the other aberrations, such as astigmatism, are unknown to the model. *Can the neural network generalise its estimations on approximated measurements in the presence of additional aberrations without retraining it?*

1.3 Problem Objective and Scope

This research aims to develop a neural network model to estimate OAM crosstalk in FSO systems using OAM modes, particularly in the presence of atmospheric turbulence-induced aberrations such as lateral displacement, tip/tilt, and other turbulence effects. The scope of this research encompasses developing and validating a neural network model for OAM crosstalk estimation under the influence of atmospheric turbulence. It includes the generation of a dataset to train and test the neural network, as well as experimental setups, simulation validations, and measurement verifications. However, the research does not mitigate OAM crosstalk. The essential contribution is developing a simple neural network model to estimate OAM crosstalk in FSO systems under atmospheric turbulence. The specific objectives of this research are:

1. Generation and validation of a comprehensive dataset that consists of lateral displacement, tip/tilt, and OAM crosstalk measurements for use in the training and validation of the neural network. This is discussed in Chapter 3.
2. Develop and evaluate a simple neural network model with optimised architecture and parameters for accurate OAM crosstalk estimation. The discussion on the development of the model is provided in Chapter 4
3. Generating a comprehensive testing dataset in the presence of turbulence with approximated lateral displacement and tip/tilt and their corresponding OAM crosstalk measurements, as elaborated in Chapter 5.
4. Evaluation of the neural network's ability to generalise to unseen turbulence conditions and estimate OAM crosstalk without retraining. This evaluation is discussed in Chapter 5.

CHAPTER 2

Background

THIS chapter serves to provide a general background needed to understand the work done for this research. OAM modes are the kind of spatial mode of light used by this research in Sec. 2.1. Atmospheric turbulence and its effects on the FSO channel will be discussed first in Sec. 2.2. The models of OAM crosstalk due to tip/tilt and displacement, as well as turbulence that guided the foundations of this research, will be in Sec. 2.3. Following this, different aspects of deep neural networks are detailed in Sec. 2.4.

2.1 Spatial Modes of Light

Maxwell's equations describe entirely the behaviour of the electromagnetic field, whose electric and magnetic parts components are, respectively, denoted as **E** and **B**. These equations (not only) permit solutions for **E** and **B**, which correspond (physically) to travelling waves. Electromagnetic fields in free space, such as laser beams, can be described by the so-called Helmholtz equation, given by

$$(\nabla^2 + nk^2)\mathbf{E} = 0 \tag{2.1}$$

where $k = \frac{2\pi}{\lambda}$ is the wave number related to the frequency of the wave, and n is the refractive index of the medium, where n = 1 in a vacuum. **E** is the vector electric field.
The wavelength is given by λ, and for visible and infrared wavelengths (for example, between 400 and 1600 nm) is on the order of hundreds of terahertz. There are cases when the electric and magnetic components of the field have similar directions at all points in space (i.e. a uniform polarisation), the electric field can be treated as a scalar field in cylindrical coordinates (and it can be expressed in Cartesian coordinates), $U(r, z)$, describing its spatially dependent behaviour. Separating the temporal and spatial behaviour simplifies Maxwell's equations to the Helmholtz equation

$$(\nabla^2 + nk^2)U(r, \phi) = 0 \tag{2.2}$$

The solutions to the Helmholtz equation above, often called modes, are determined by the chosen coordinate system and boundary conditions. Under the paraxial approximation (the limit of slight beam divergence in the traverse plane), it can be assumed that the waves propagate primarily in the z-direction, with a spatial extent in the transverse (x-y plane)

much smaller than the propagation distance, thus simplifying the original second-order Helmholtz equation into a first-order partial differential equation

$$U(r,\phi,z) = U(r,z)\exp^{\ell\phi} \tag{2.3}$$

where ϕ and r are the azimuthal and radial coordinates, ℓ is an azimuthal charge, and $U(r,z)$ is the radial profile of the beam (mode). The Gaussian mode is the fundamental mode of most laser sources. However, the Gaussian profile is not always ideal for some applications, such as MDM. In such cases, it becomes necessary to have multiple channels in different spatial modes that might carry information. In this section, we discuss LG modes, OAM modes in particular, and the methods used to generate and detect them. Most equations used in this section about spatial modes of light and modal decompositions are originally derived in Ref [44].

2.1.1 Gaussian Mode

The paraxial wave equation yields a Gaussian beam as one of its solutions. A Gaussian intensity profile characterises this beam and exhibits a uniform phase across the transverse (xy) plane when $z = 0$. The field describing a Gaussian beam is given by

$$U(r,z) = \frac{1}{z + jz_R}\exp\left(\frac{-r^2}{\omega^2(z)}\right)\exp\left(\frac{-j\pi r^2}{\lambda R(z)}\right) \tag{2.4}$$

where z is the distance to the beam's focus and r, is the radial position. There is no azimuthal dependence as a Gaussian beam is radially symmetric. The radius of the beam is ω, which is the point at which the field amplitude drops to $1/\mathrm{e}$ (or intensity $1/e^2 \approx 13.5\%$) of the axial value, and as a function of z is

$$\omega(z) = w_0\sqrt{1 + \frac{z^2}{z_R^2}} \tag{2.5}$$

The Rayleigh range,z_R^2, defined as the distance where the beam area doubles and is a measure of the tightness of the focus, is given by $z_R^2 = \frac{\pi\omega_0^2}{\lambda}$. The radius of curvature of the wavefront as a function of zis

$$R(z) = z\left(1 + \left(\frac{z_R}{z}\right)^2\right) \tag{2.6}$$

If $z \ll z_R$, the beam is collimated, implying a flat wavefront, and the beam radius is approximately constant. If $z \gg z_R$, the beam diverges, implying a spherical wavefront with a radius of curvature $R(z) \approx z$.

2.1.2 Laguerre-Gaussian Modes

Several other solutions exist for the paraxial wave equation describing laser fields, such as Gaussian beams and higher-order Hermite–Gaussian (HG) modes. Of particular interest to this work are the Laguerre–Gaussian solutions, which are best expressed in cylindrical polar coordinates (ρ,ϕ,z) and take the form

$$U(r,\phi,z) = C_{\ell p}(\sqrt{2}\frac{r}{\omega(z)})^{\ell}L_p^{\ell}(\frac{2r^2}{\omega(z)^2})\frac{\omega_0}{\omega(z)}\exp[-i\psi_{p\ell}(z)] \times \exp[i\frac{k}{2q(z)}r^2]e^{i\ell\phi} \tag{2.7}$$

where $L_p^{\ell}(\cdot)$ is the associated Laguerre polynomial, $C_{\ell p}$ is a normalisation constant, $\omega(z)$ is the beam radius, ω_0 is the beam radius at the beam waist, $z_0 = \frac{\pi\omega_0^2}{\lambda}$ is the Rayleigh range,

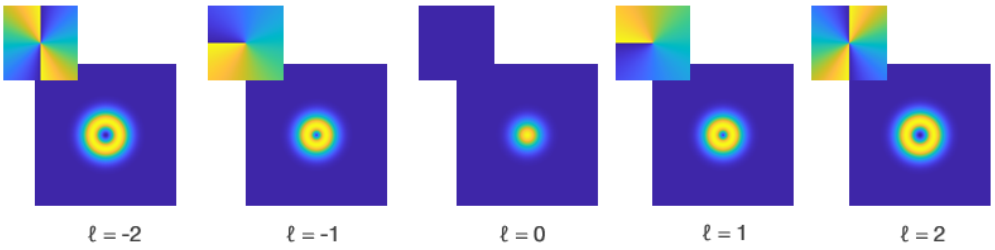

Figure 2.1: Intensity patterns with inset phase of Laguerre-Gaussian (only OAM modes indicated where $p = 0$).

$q(z) = z - iz_0$, is the complex beam parameter and $\psi_{p\ell}(z) = (2p + |\ell| + 1)\tan^{-1}\left(\frac{z}{z_0}\right)$ is the Gouy phase shift. The normalisation constant, $C_{\ell p}$ is given by

$$C_{\ell p} = \sqrt{\frac{2p!}{\pi(p + |\ell|)!}} \tag{2.8}$$

The most significant part of this lengthy expression is the azimuthal phase dependence in the term $e^{i\ell\phi}$. This small-looking term tells us there is a twist in the phase, indicating the existence of a phase vortex at $p = 0$; if we travel along a circular closed path around this axis, then we accumulate a phase twist of $2\pi\ell$. This azimuthal phase dependence suggests that a Laguerre–Gaussian laser beam, as described in Equation (2.8), possesses OAM of ℓh per photon. OAM is a property in both intense laser beams within the classical domain and individual photons. The remaining p element is associated with the beam's broadening due to diffraction. This azimuthal phase dependence indicates that a Laguerre–Gaussian laser beam of the form Equation (2.8) carries OAM. Hence, the OAM modes are a subset of LG modes with $p = 0$.

OAM beams are defined by the azimuthal index, ℓ, with any number of integer twists [11]. The recent developments in OAM have mainly been due to its use in optical communications and information transfer. This is because OAM modes, being a subset of LG beams, are orthogonal to each other, making them useful for multiplexing [45]. OAM modes are generated on a Spatial Light Modulator (SLM) using a suitable grating, such as a blazed grating encoded with LG modes at $z = 0$. Figure 2.1 displays examples of Laguerre-Gaussian modes with various azimuthal (ℓ) and $p = 0$, indicating the OAM modes. We consider only LG modes with radial index $p = 0$ throughout the work. The orthogonality of the modes has been seen to increase the channel capacity of optical communication channels. These modes can be generated by digital holograms encoded on SLMs and Digital Micromirror Device (DMD)s.

2.1.3 Mode Characterization by Modal Decomposition

In a free-space optical system, detecting Gaussian beams using a photodiode is simple. OAM modes have a ring-shaped profile even when focused, often placing the photodiode in the dark central region of the ring. This becomes particularly important in an MDM system using multiple modes, where the task is to separate and direct these modes to individual photodiodes. A modal decomposition is a powerful tool to characterise or unravel optical fields according to their constituent modes. This technique can reveal the information of crosstalk present in a particular LG field in an optical system. Modal decomposition involves determining the weighted sum of modes of an individual basis mode set constituting a given field by measuring the amplitude weightings and relative phases of these modes [44].

Any unknown field, $U(\mathbf{s})$, can be written as a sum of modes which are an orthonormal basis set, $\Psi_n(\mathbf{s})$, expressed as

$$U(\mathbf{s}) = \sum_{n=1}^{\infty} c_n \Psi_n(\mathbf{s}) = \sum_{n=1}^{\infty} |c_n| e^{i\phi_n} \Psi_n(\mathbf{s}), \tag{2.9}$$

with complex weights $c_n = |c_n| e^{i\phi_n}$ where $|c_n|^2$ is the power in mode $\Psi_n(\mathbf{s})$ and ϕ_n is the inter-modal phase, satisfying $\sum_{n=1}^{\infty} |c_n|^2 = 1$. This research did not consider the inter-modal phase, simplifying the modal decomposition requirements. Equation (2.9) can ideally be considered the sum of several multiplexed modes, each of which is a separate communication channel. Measurement of these weightings is the core of modal decomposition and is achieved by finding the inner product of the unknown field and each basis element given by

$$c_n^2 = |\langle \Psi_n | U \rangle|^2 \tag{2.10}$$

In a practical sense, a hologram used for the inner product calculation is known as a match or correlation filter. It measures the correlation signal between the unknown incoming mode, $U(\mathbf{s})$, and the function encoded within the hologram, Ψ_n.

The inner product can find the unknown modal coefficients, c_n, which carry the modulated information, which the inner product can see. The unknown modal coefficients can be obtained by

$$c_n = \langle \Psi_n | U \rangle = \int \Psi_n^*(\mathbf{s}) U(\mathbf{s}) d\mathbf{s}, \tag{2.11}$$

where we have exploited the ortho-normality of the basis, namely

$$\langle \Psi_n | \Psi_m \rangle = \int \Psi_n^*(\mathbf{s}) \Psi_m(\mathbf{s}) d\mathbf{s} = \delta_{nm}. \tag{2.12}$$

Note that Dirac notation, borrowed from quantum optics, has been used for the inner products. The calculation of Equation (2.12) may be achieved experimentally using a lens to execute an optical Fourier transform, $\mathcal{F}$. Accordingly we apply the convolution theorem (using $\mathbf{k}$ as an auxiliary variable)

$$\mathcal{F}\{f(\mathbf{s})g(\mathbf{s})\} = F(\mathbf{k}) * G(\mathbf{k}) = \int F(\mathbf{k}) G(\mathbf{s} - \mathbf{k}) d\mathbf{k} \tag{2.13}$$

To the product of the incoming field modulated with a transmission function (for example, a hologram), $T_n(\mathbf{s})$, that is the conjugate of the basis function, namely,

$$W_0(\mathbf{s}) = T_n(\mathbf{s}) U(\mathbf{s}) = \Psi_n^*(\mathbf{s}) U(\mathbf{s}), \tag{2.14}$$

to find the new field at the focal plane of the lens as

$$W_f(\mathbf{s}) = A_0 \, \mathcal{F}\{W_0(\mathbf{s})\} = A_0 \int \Psi_n^*(\mathbf{k}) U(\mathbf{s} - \mathbf{k}) d\mathbf{k} \tag{2.15}$$

Here $A_0 = \exp(i4\pi f/\lambda)/(i\lambda f)$ where f is the focal length of the lens and λ is the wavelength of the light. If we set $\mathbf{s} = \mathbf{0}$, which experimentally is the on-axis intensity in the Fourier plane, then Equation (2.15) becomes

$$W_f(\mathbf{0}) = A_0 \int \Psi_n^*(\mathbf{k}) U(\mathbf{k}) d\mathbf{k} \tag{2.16}$$

which is the desired inner product of Equation (2.11). Therefore, we can find our modal weightings from an intensity measurement of the on-axis light

$$|W_f(\mathbf{0})|^2 = |A_0|^2 |\langle \Psi_n | U \rangle|^2 = |c_n|^2. \tag{2.17}$$

In practice, transmission functions are encoded onto SLM, essentially digital holograms. Systems often have multiple modes of interest. Multiple holograms can be cycled on the SLM in a time division multiplexed manner to detect all modes. Alternatively, they can be combined with distinct grating functions, allowing spatial separation of the "spots" representing each mode. The on-axis intensity must be measured precisely, excluding any surrounding light or misalignments; otherwise, crosstalk will be introduced.

2.2 Atmospheric Turbulence

Laser systems travelling through free space inevitably experience degradation due to atmospheric turbulence and other weather-related factors. While weather effects could be mitigated under ideal conditions, turbulence effects are unavoidable. Weather impacts are mainly dependent on the wavelength. Turbulence arises primarily from fluctuations in temperature and pressure, leading to spatial and temporal changes in the refractive index structure. When a Gaussian beam encounters turbulence, three main effects occur: beam spreading, causing the beam to expand; beam wander, altering the beam's centroid position at the receiver; and scintillation, which changes the beam's shape due to intensity fluctuations. Additionally, beams that contain OAM will disperse their energy to neighbouring modes, resulting in OAM crosstalk when propagating through turbulence.

2.2.1 Kolmogorov Model

When a laser beam propagates through the atmosphere, it encounters spatially varying diffractive indices caused by air pockets with different temperatures. The refractive index of the atmosphere is not uniform. It consists of a multitude of eddies of various sizes, each with varying indices of refraction. As a laser beam propagates through the atmosphere, these variations will distort its wavefront. The variations are caused by temperature fluctuations that arise from the turbulent mixing of various thermal layers. The average size of the turbulent eddies can be specified by an inner scale, l_0, which is typically on the order of millimetres, and an outer scale, L_0, which is on the order of meters [18]. The Kolmogorov model for turbulent flow is the basis for many contemporary turbulence theories and can relate these temperature fluctuations to refractive index fluctuations. Kolmogorov turbulence assumes that solar heating and wind shear provide energy on large scales (the outer scale, L_0), and it is dissipated as heat by viscous action of the air to the smaller eddies (inner scale, l_0) [46]. The power spectral density of the refractive index fluctuations given by the Kolmogorov model is described by [46]

$$\Phi_n^K(k) = 0.033 C_n^2 k^{-11/3} \quad \text{for} \quad 1/L_0 \ll k \ll 1/l_0 \tag{2.18}$$

Values of C_n^2 vary from $10^{-17}\,\mathrm{m}^{-2/3}$ in weak turbulence and up to about $10^{-13}\,\mathrm{m}^{-2/3}$ in strong turbulence [18]. Kolmogorov's turbulence theory assumes a homogeneous, isotropic atmosphere independent from large-scale turbulence. Various turbulence power spectrum models exist, including the Hill power spectrum ((which has no analytical solution), the Tatarskii power spectrum, and the von Kármán power spectrum. The Tatarskii power spectrum considers both the inner scales [18]. The von Kármán spectrum adds the effect of both the inner and outer scale eddies to the Kolmogorov model [18]. The Modified Atmospheric Spectrum combines aspects of the von Kármán and Hill spectra [18] and temperature's influence. These models introduce modifications of the Kolmogorov spectrum that suppress low spatial frequencies [47]. We use the Kolmogorov model in this work because it accounts for the low-order aberrations of interest, such as tip and tilt.

2.2.2 Beam Wander

Beam wander refers to the movement of the point of maximum intensity over the receiver plane. This phenomenon is caused by large-scale eddies that are inhomogeneous due to their different refractive effects and turbulent eddies that are much larger than the diameter of the beam [18, 48]. As a result, the beam randomly wanders about the centre of the detector over a long period, resulting in a beam with a large area, also known as the long-term beam size. This long-term beam size is Gaussian-like on average due to smaller short-term beam wandering [49]. The long-term beam size, denoted as ω_{LT}, is determined by [18]

$$\omega_{LT}^2 = \omega_{LT}^2 + r_c^2 \tag{2.19}$$

This phenomenon shifts the central point, potentially causing a significant signal loss in applications such as free-space optical communication. In extreme situations, this shift may lead to the beam missing the receiver aperture or the detector's focal spot due to beam wander.

The statistical model for beam wander at the receiver plane follows a Gaussian distribution, characterised by a long-term average radial variance denoted as r_c^2, and the size of the received beam without any averaging, known as the short-term beam [18]. Numerous analytical solutions have been developed to determine the beam wander radial variance. In the case of infinite outer scale Kolmogorov turbulence, the beam wanders radial variance for a collimated beam with beam waist radius, ω_0, is expressed as

$$r_c^2 = 2.42 C_n^2 L^3 \omega_0^{-1/3} \tag{2.20}$$

On the other hand, angle-of-arrival fluctuations are associated with image jitter in the focal plane of an imaging system cause. This effect is caused by the wavefront tilt (i.e. phase structure) at the receiver produced by atmospheric turbulence [18, 50]. The angle-of-arrival variance is directly related to the beam centroid variance (wander) about the mean point of arrival. Variations in the angle-of-arrival and beam wander can influence system performance through such effects as pointing error and signal strength variations [51]. Beam wander at the receiver plane can be modelled as if it arises from a random tilt angle at the transmitter plane, similar to angle-of-arrival fluctuations of a reciprocal propagating wave with the receiver diameter replaced by the transmitter beam diameter [52].

2.2.3 Beam Spreading

Beam spreading results from small-scale fluctuations, which causes the beam power to distribute over a large surface area. This spread reduces the intensity and energy that is received by optical systems. In the absence of turbulence, the spread of the laser beam will depend on the diameter of the transmitting aperture D. For a diffraction-limited transmitter, the angular spread θ of the beam in the far field is given by $2\lambda/\pi D$, where λ is the wavelength of the beam. Through turbulence, the spread becomes much more significant than θ at the receiver plane due to scattering by the moving turbulent eddies. The total spread of the beams comprises two effects: beam wander, which results from larger turbulent eddies, and beam broadening, which results from eddies smaller than the transmitting aperture D [18]. The latter, also termed short-term beam spread, depends on a parameter referred to as the lateral coherence length or the Fried parameter r_0. It is a helpful alternative to C_n^2 for a plane wave (approximately a collimated Gaussian beam) in Kolmogorov turbulence, given by [18]

$$r_0 = 1.68(C_n^2 L k^2)^{-3/5} \tag{2.21}$$

where k is the wave number and L is the propagation path length. If the beam diameter D is much smaller than r_0, the effect of turbulence on the beam is negligible, and the diameter of the spread will solely depend on θ. However, if the transmitting diameter is much larger than the coherence length, the diameter of the spread will depend on r_0 in the form of $\theta = 2\lambda/\pi D$, where λ denotes the wavelength.

2.2.4 Scintilation

Atmospheric turbulence causes fluctuations in intensity in addition to fluctuations in beam size and position. This effect is referred to as scintillation. When a laser beam propagates through the atmosphere and encounters refractive-index inhomogeneities produced by

small eddies far smaller than the beam diameter in the atmosphere, the result is scintillation. Random spatially and temporally random intensity distributions are received at the receiver plane, manifesting as random beam wavefront phase aberrations and intensity deformations, leading to mode crosstalk — a significant challenge for MDM. The scintillation index is used to characterise the strength of scintillation and is given by

$$\sigma^2 = \frac{\left\langle I^2(\mathbf{0}) \right\rangle - \left\langle I(\mathbf{0}) \right\rangle^2}{\left\langle I(\mathbf{0}) \right\rangle^2}, \tag{2.22}$$

where $\left\langle I(\mathbf{0}) \right\rangle$ and $\left\langle I^2(\mathbf{0}) \right\rangle$ are the first and second moments, respectively, of an ensemble of intensities detected by the point detector after propagating a distance L. The scintillation index may be used to characterise turbulence strength roughly. Weak turbulence is when $\sigma^2 < 0.3$, medium is when $\sigma^2 \approx 1$, and strong is when $\sigma^2 \gg 1$. Strehl Ratio (SR) is another common parameter similar to the scintillation. The SR value can be used to characterise turbulence strength. It is the ratio of the average on-axis beam intensity with $\left\langle I(\mathbf{0}) \right\rangle$, and without Kolmogorov turbulence, $I^0(\mathbf{0})$, given by

$$\mathrm{SR} = \frac{\left\langle I(\mathbf{0}) \right\rangle}{I^0(\mathbf{0})} \approx \frac{1}{\left[1 + (D/r_0)^{5/3}\right]^{6/5}} \tag{2.23}$$

where D is the beam's diameter, and r_0 is the coherence. SR uses values from 0 to 1, covering strong to weak turbulence. Scintillation can be reduced by averaging aperture, where the beam's receiving aperture is increased to statistically average the independent portions of the scintillated beam [18].

2.3 OAM Modal Crosstalk Models

The modelling of turbulence-induced crosstalk is complicated and not extensively researched. Crosstalk stands as an essential metric for MDM channels, and thus, it has been studied in some detail, both empirically and analytically, particularly concerning OAM modes [22, 23, 53, 54]. Within an MDM system, turbulence causes crosstalk between modes due to the wavefront aberrations, an aspect explored within misalignments and turbulence. Various models in the literature shed light on these phenomena.

The spatial degree of freedom experiences aberrations, leading to mode coupling with neighbouring modes and compromising their orthogonality. The degree of crosstalk depends on the strength of the channel's turbulence. A significant source of crosstalk error in MDM systems arises from lateral displacement and tip/tilt at the receiver [40, 41, 55]. Lateral displacement can stem from the movement of both transmitter and receiver platforms and atmospheric turbulence. It is important to note that lateral displacement can co-occur with tip/tilt (angular error), also known as pointing error [56].

2.3.1 Tip/Tilt and Displacement

Typically, a laser beam can experience two forms of misalignment concerning a reference axis: lateral displacement and tip/tilt. Misalignment occurs when a reference axis other than the beam's propagation direction is used. Figure 2.2 illustrates lateral displacement and tip/tilt on a beam with respect to a measurement axis. Because OAM is extrinsically defined, even slight misalignments can significantly affect the OAM spectrum [41]. Simulations and experiments have been done to demonstrate the effect of tip/tilt and lateral displacement on LG beams in terms of OAM spectra using modal decomposition. There is a general analytical expression on a Gaussian for the weight of the OAM mode given by [40]

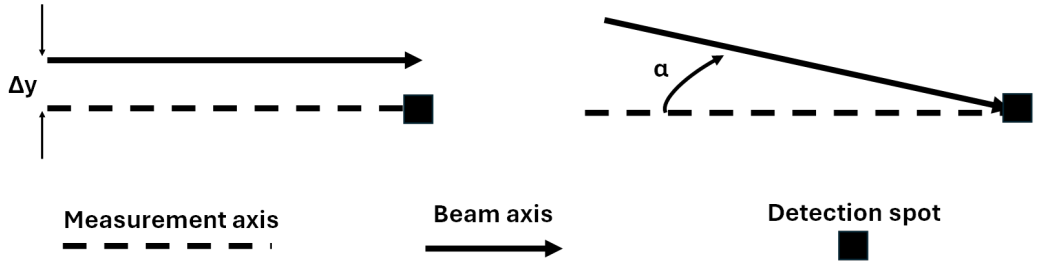

Figure 2.2: Illustration of lateral displacement and tip/tilt angle. The beam axis is the axis on which the beam propagates. The measurement axis is the axis at which the intensity of the beam is measured at the detector spot. Lateral displacement, Δy, is the offset of the beam axis vertically (or horizontally) parallel to the measurement axis. Tip/Tilt, α, is when the beam axis is at an angle upon beam arrival at the detector spot. Therefore, lateral displacement and tip/tilt cause the beam axis to be misaligned with the measurement axis.

$$c_\ell(u_0, v_0) = \exp\left(-\frac{u_0^2+v_0^2}{4}\right)\left(\frac{\sqrt{u_0^4+v_0^4+2u_0^2v_0^2}}{u_0^2+v_0^2}\right)^{\ell} I_\ell\left(\frac{\sqrt{u_0^4+v_0^4+2u_0^2v_0^2}}{u_0^2+v_0^2}\right) \tag{2.24}$$

where c_ℓ is the weight of the ℓ-th mode, $u_0 = \frac{2\Delta y}{\omega_0}$ and $v_0 = \frac{2\pi\omega_0 sin\alpha}{\lambda}$. Δy and α are the lateral displacement and tilt angle measured, respectively. $I_\ell(x)$ is the nth-order modified Bessel function of the first kind.

2.3.2 Turbulence Induced

Previous studies have reported a more general analytic expression to calculate normalised average received power on different OAM orders, P(ℓ) [57]. This approximation further allows obtaining a closed-form expression for P(ℓ)

$$\mathrm{P}(\ell) \approx \frac{\beta^\ell \cdot {}_2F_2\left(\frac{1}{2}+\ell, 1+\ell; 2+\ell, 1+2\ell; -2\beta\right)}{2^\ell \Gamma(2+\ell)} \tag{2.25}$$

where $\Gamma(\cdot)$ is the gamma function and ${}_2F_2$ is the generalised hypergeometric function and $\beta = 1.8025(D/r_0)^{5/3}$. The equation is an approximated formula that only considers the low-order turbulence aberrations from Zernike terms (e.g., tip and tilt). This approximation is based on the contribution to the OAM modal coupling of higher-order aberrations, which diminishes rapidly and can be orders of magnitude smaller [57]. It has been shown that Equation (2.25) generally underestimates P(ℓ), but it is in relatively close agreement with the exact values for ℓ = 0,1.

The OAM modal crosstalk was calculated by considering Kolmogorov statistical models of atmospheric turbulence. $\langle P_\triangle \rangle$ is the ensemble average of the fraction of the received power that is found to be in OAM mode specified by $\ell_j = \ell_i + \triangle$ when mode ℓ_i is transmitted is given by [22]

$$\langle P_\triangle \rangle = \begin{cases} 1 - 1.01\left(\frac{D}{r_0}\right)^{5/3} & \text{for } \triangle = 0, \\ 0.142\frac{\Gamma(\triangle - \frac{5}{6})}{\Gamma(\triangle + \frac{11}{6})}\left(\frac{D}{r_0}\right)^{\frac{5}{3}} & \text{otherwise.} \end{cases} \tag{2.26}$$

The above equation was previously confirmed to be accurate, but recent findings have revealed its inaccuracy over longer distances (1.7 km), likely attributed to beam wander [58].

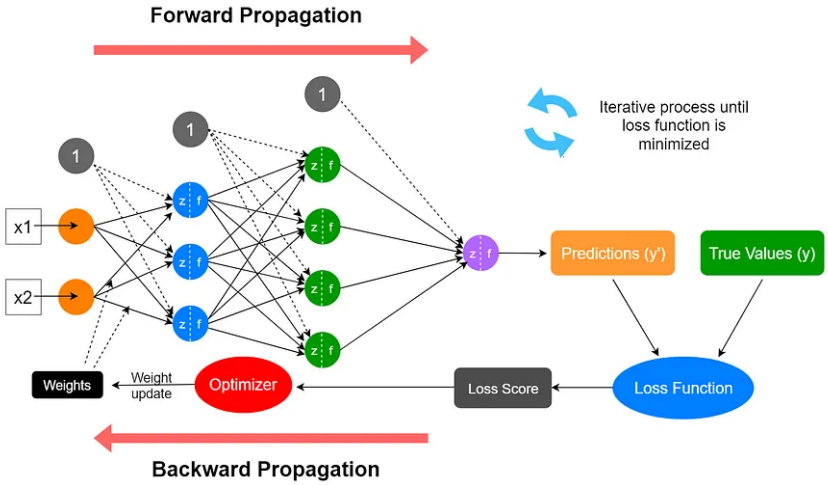

Figure 2.3: Architecture of a feedforward neural network structure showing the inputs, hidden and output layers. The neural network learning process is shown, illustrating the forward propagation of inputs through hidden layers to output, backward propagation of error, weight optimisation, and loss calculation with model estimations and true values.

2.4 Deep Neural Networks

2.4.1 Architecture

Deep Neural Network (DNN)s have different architectures used to solve various problems. Examples of DNN architectures include Feedforward Neural Network (FFNN), Convolutional Neural Network (CNN), and Recurrent Neural Network (RNN). In this research work, a feedforward neural network was used. The typical structure of a FFNN is shown in Figure 2.3. A FFNN is shown in the figure and has the following major parts:

Input Layer

A layer that comprises input data features or representation.

Input Weights

Weights of the connections between the input layer and the first hidden layer of the network.

Hidden Layers

The layers of neurons between the input and output layers. They are used to learn the relationship between the input and output signals.

Hidden Neurons Weights

Weights of the connections between the hidden layers.

Output Weights

Weights between the last hidden layer and the output layer.

Output Layer

The last layer of a network. It gives the output of the network from network inputs.

2.4.2 Activation Functions

Real-world data is usually nonlinear. The purpose of activation functions is to introduce non-linearities into the network [59]. Non-linearities allow the neural networks to approximate patterns in arbitrarily complex functions. This is important because linear activation functions produce linear output regardless of network size. Some examples of activation functions and equations obtained from Ref [60] that were considered for use in this work are:

Sigmoid function

The sigmoid activation function is nonlinear, meaning the outcome is nonlinear. This function is beneficial because it is easy to compute its derivative. It has a range of values between 0 and 1. Their range makes them useful in tasks where the output needs to be a probability distribution.

$$\sigma(x) = \frac{1}{1 + e^{-x}} \tag{2.27}$$

Rectified Linear Unit (ReLU) Activation

The ReLU activation function is a nonlinear function defined as the maximum between 0 and the input max(x). It is widely used in neural networks for its simplicity and good performance obtained using different architectures and datasets.

$$\text{ReLU}(x) = \max(0, x) \tag{2.28}$$

Hyperbolic Tangent (Tanh)

The hyperbolic tangent function squashes the input values between -1 and 1. It looks like a sigmoid function; the difference is the symmetry around the origin. The range of output values makes it helpful in normalising inputs and when the outputs can be negative or positive.

$$\tanh(x) = \frac{e^{x} - e^{-x}}{e^{x} + e^{-x}} \tag{2.29}$$

Softmax

The softmax function squashes the input values into the range [0, 1] and ensures that the resulting values sum up to 1, making it suitable for generating probabilities for multiple classes. It is often used as the final activation function in the output layer of multi-output neural networks.

$$\text{Softmax}(x_i) = \frac{e^{x_i}}{\sum_{j=1}^{N} e^{x_j}} \tag{2.30}$$

2.4.3 Training Process

Deep neural networks are powerful tools in modern machine learning, and how they learn is crucial. The training aims to find the neural network that minimises the error (loss) between the model's estimated outputs and the actual (target) values averaged across the entire

dataset. This implies finding the weights that, on average, give the smallest loss possible. Below, we will discuss three key parts of their learning process: forward propagation, loss functions, and backpropagation.

Forward propagation

In a neural network such as FFNN architecture, computation is a sequence of operations on the output of a previous layer. The final operations generate the output. For a given input, the output stays the same; it does not depend on the last input network. The neural network's estimated output is compared with the expected output, and the loss is determined.

Loss Functions and Performance Metrics

The loss of a network measures the cost incurred by the model from incorrect estimations; therefore, they are used to train the neural network. The loss function is a function of the weights of the network. The gradient of the loss function concerning the output is then determined. The problem determines the choice of the loss function to use, whether it is a regression or a classification task. In this work, we model OAM crosstalk as output continuous real numbers. In regression problems, the commonly used loss functions are Mean Square Error (MSE), Root Mean Square Error (RMSE), and Mean Absolute Error (MAE) [61]. Assuming the model output be $\hat{y} = \{\hat{y}_1, \hat{y}_2, \ldots, \hat{y}_n\}$ and actual (target) values be $y = \{y_1, y_2, \ldots, y_n\}$. These loss functions considered are

1. **Mean Squared Error (MSE)**:

$$\text{MSE} = \frac{1}{N}\sum_{i=1}^{N}(y_i - \hat{y}_i)^2 \tag{2.31}$$

2. **Average Root Mean Squared Error (RMSE):**

$$\text{RMSE} = \sqrt{\frac{1}{N}\sum_{i=1}^{N}(y_i - \hat{y}_i)^2} \tag{2.32}$$

3. **Mean Absolute Error (MAE):**

$$\text{MAE} = \frac{1}{N}\sum_{i=1}^{N}|y_i - \hat{y}_i| \tag{2.33}$$

Backpropagation

A loss function of a neural network is composed of weights from successive layers between input and output layers [62]. Backpropagation uses the chain rule to obtain the gradient of the loss function in terms of the summation of local gradient products over different node connections between input and output layers [63, 64]. The gradient is computed from the output layer backwards. Backpropagation determines how much a small weight change will affect the loss function. Backpropagation algorithms typically use gradient-based optimisation algorithms to update the neural network parameters on each layer.

Optimisers

Training a network is complicated even though the backpropagation is simple because a network has several weights. Therefore, optimisers are used to optimise the loss function.

The optimiser defines the magnitude and speed of each parameter update by setting the learning rate [59, 65]. The learning rate guides how the gradient of the loss function adjusts the network's weights during backpropagation. They optimise the process of minimising the error by adjusting the weights based on the gradients of the loss function. Optimisation is done to define a function that makes the solution through DNN networks easier by finding the values of the parameters that minimise a loss function. The optimisers considered during the model development stage are Adam, SGD, AdaDelta, Adagrad, and RMSprop [66].

CHAPTER 3

OAM Crosstalk Measurements Validation: Experiment vs. Simulation

BEAM wander and angle-of-arrival fluctuations are well-modelled phenomena in atmospheric turbulence that have a direct influence on modal crosstalk. Understanding the turbulence-induced beam wander is crucial for understanding crosstalk dynamics in free-space communication. Previous research has investigated the effects of lateral displacement and tip/tilt on laser beams, particularly Gaussian mode and LG beams. Two methods have emerged to characterise these effects. The first method offers an analytical expression for crosstalk in Gaussian mode, with implications extendable to higher modes, as suggested by the authors. One such study models the detected OAM spectrum resulting from misalignment, encompassing tip/tilt (α and β) and lateral displacement (x and y), of a Gaussian mode (specifically, the $\ell = 0$ mode) incident on a detection hologram. The OAM spectrum was derived in Ref [40], as represented by Equation (2.24).

The second method offers an expression for the modal decomposition of both Gaussian and higher modes, facilitating the calculation of crosstalk. This approach entails decomposing the misaligned beam into a series of LG modes with varied topological charges and relative intensities. The OAM spectrum is then derived by computing the inner product between the misaligned beam and each LG mode. This spectrum provides a quantitative assessment of the distribution and relative intensities of OAM modes, offering insights into the impact of misalignment. Such analysis can be conducted through either experimental approaches or simulation.

Several studies have used the second method to explore the effects of lateral displacement only [67, 68], tip/tilt only [69], and both simultaneously on the crosstalk of LG beams [41, 70]. While simulations have provided insights into the spectrum of misaligned LG beams, corresponding experimental results are lacking [41]. However, ambiguities arise with the expressions provided. Firstly, each of the three misalignment cases (displacement only, tip/tilt only, and both) requires a distinct expression, resulting in complexity in their application. Secondly, inconsistencies are evident in the notation used, particularly regarding the sign of ℓ, within these expressions.

The existing literature shows that analytical expressions are available to determine the OAM crosstalk due to tip/tilt and displacement for a Gaussian mode. These closed-form expressions for OAM crosstalk present a challenge when conditions change, such as when considering the effects of turbulence, making it challenging to incorporate these changes

into the expressions. In real-world free-space systems, misalignments and turbulence effects contribute to OAM crosstalk, causing closed-form solutions to be less suitable for systems with turbulent conditions. However, using machine learning techniques may offer a potential opportunity for incorporating these changes effectively.

This chapter focuses on validating the generated dataset for neural networks. We will utilise analytical expressions from existing literature to develop the OAM beams and control the tip/tilt and displacement amounts. Subsequently, we will measure the corresponding OAM crosstalk using modal decomposition to create the training dataset. Acknowledging the fundamental importance of training data for the success or failure of neural networks, this chapter undertakes a comprehensive discussion on data generation and validation. Neural Network (NN) training or development is not covered in this chapter.

3.1 Experimental Setup and Methodology

The experimental setup depicted in Figure 3.1 employs a He-Ne laser emitting light at a wavelength of 632.8 nm. The laser beam undergoes collimation and expansion before being directed onto one half of a phase-only SLM (Holoeye, PLUTO-2.1) to generate LG modes with a beam waist of $\omega_0 = 0.34$ mm. Subsequently, the LG modes are imaged by a 4f imaging system comprising lenses f3 and f4, followed by passage through the system of two beam splitters, (BS). The 4f imaging system and a spatial filter selected the first diffraction order after the SLM. 50% of the beam from the BS1 propagates a distance of 975 mm to the other half-side of the SLM for modal decomposition using the Fourier lens and the camera (for detailed guidance, refer to [44]), while the remaining 50% of the beam from the BS1 proceeds to the BS2. The remaining 50% of the beam from BS1 proceeds to the BS2 for offset measurement due to displacement and tip/tilt.

In the experimental setup, the OAM modes were encoded on holograms displayed on the SLM with displacement and tip/tilt being introduced during mode generation using [41]

$$U(x,y) = U^{LG}(x+\Delta x, y+\Delta y)\exp\left(i\frac{2\pi}{\lambda}\left(x\sin\alpha + y\sin\beta\right)\right) \tag{3.1}$$

Lateral displacement misalignment is achieved by adding random lateral displacements Δx and Δy along the x and y directions, respectively, in Equation (3.1). For tip/tilt, x and y tip/tilt components (i.e., α and β) are added to the phase term of the beam in Equation (3.1) along the x and y directions, respectively. The ranges of displacement and tip/tilt, both in the x and y directions, are set at [-2ω_0, 2ω_0] and [-0.025°, 0.025°], respectively. Various techniques have been employed to impose tip/tilt and displacement on OAM beams [40, 41].

Cameras 1 and 2 measure the offset when there is displacement and tip/tilt, respectively, on the beams from the second beam splitter. Tip/tilt and displacement combinations are generated through random sampling from a uniform distribution within the specified ranges to minimise biases in the training dataset. Input modes considered range from $\ell_{\text{input}} =$ -5 to 5. During the measurement of OAM spectra using modal decomposition, the mode bases for detection range from $\ell =$ -10 to 10 for all input modes to prevent leakage of normalised power(i.e. mode coefficient weights) during the modal decomposition process.

3.2 Displacement and Tip/Tilt Dataset

A simulation was conducted based on the setup depicted in Figure 3.1, employing Equation (3.1) for OAM beam generation and tip/tilt and displacement control. This simulation served to validate the experimental measurements. The simulation used uniformly distributed variations of tip/tilt and lateral displacement to generate a training dataset for

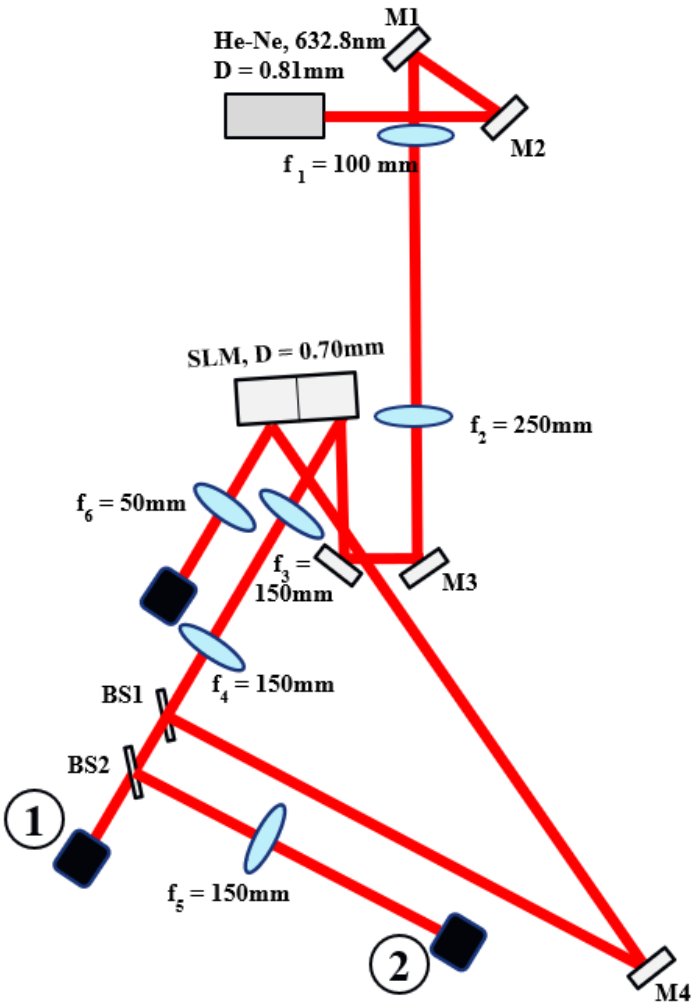

Figure 3.1: The experimental setup used in this work is equivalent to the simulation setup used to perform a modal decomposition. The beam splitters, BS1 and BS2, direct the beam to the SLM for modal decomposition and to the two cameras to measure the tip/tilt and displacement values. Cameras 1 and 2 are used for displacement and tip/tilt measurements.

the neural network to produce corresponding OAM spectra. Subsequently, the simulation results were compared with experimental OAM spectra measurements obtained under identical tip/tilt and displacement values. The simulation significantly accelerated the generation of OAM spectra for a single misalignment combination, completing the task in only 20 seconds, compared to the 3-minute duration for experimental measurements. A training dataset requiring thousands of measurements required several days of continuous experimentation using experimental modal decomposition. During the experimental phase, one key challenge was the difficulty in controlling misalignments introduced within the setup, mainly as environmental factors such as room temperature fluctuations or laboratory movements could induce variations over days. Consequently, leveraging the simulation proved instrumental in generating a robust training/validation dataset for the neural network. The size of the dataset was increased during model training and optimization for better results. The final dataset had 21153 (1923 misalignment combinations) rows for the combination of misalignments and input modes, ℓ_{input}, and their corresponding OAM

spectra.

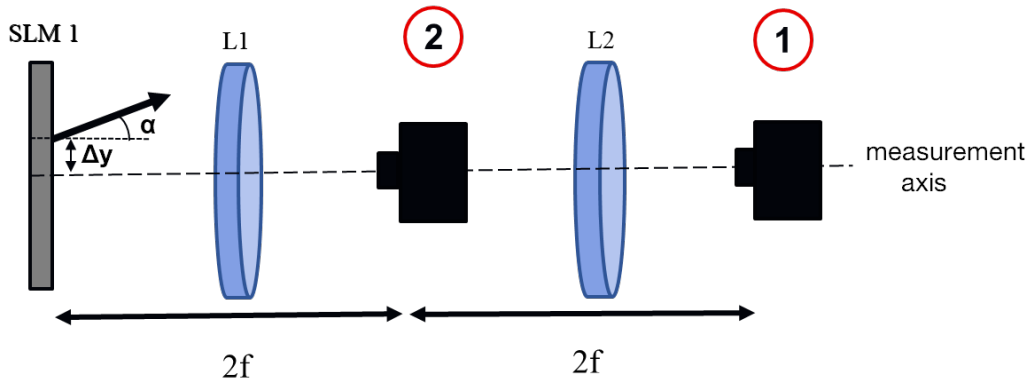

Figure 3.2: Experiment schematic of how the SLM is used to impose both lateral displacement and tip/tilt angle on the first SLM hologram. During mode creation, the SLM-imposed lateral displacements and tip/tilt are achieved by specifying values of Δx, Δy, β α. Displacement was measured using the camera at the 4f point, position 1. The camera at the 2f point measured the offset caused by tip/tilt that is used to calculate tip/tilt.

We experimentally verified the tip/tilt and displacement values by encoding them on the hologram displayed to the SLM using Equation (3.1) and measuring the imposed misalignment values, respectively, at camera positions 1 and 2. Figure 3.2 illustrates how and where the measurements of tip/tilt and lateral displacement were made in the setup. Both lateral displacement and tip/tilt angle are determined with respect to the measurement axis. The measurement axis is determined before any SLM-imposed misalignments are performed and acts as a reference point for the measurements. This was done to check if the experiment was optically performing tip/tilt and lateral displacement at the receiver as encoded at the SLM during beam creation. This verification was important as it assessed if the camera could correctly measure what was encoded on the SLM as tip/tilt or lateral displacement at their respective positions. Verifying the encoded tip/tilt and lateral displacement involved two steps. The camera had a pixel size of 3 mm, and each lens was used before the camera focused on the local wavefront on the image sensor plane. To verify the encoded displacement, the first step was to encode a Gaussian mode on the first half side of the SLM and observe the first-order Gaussian beam's movement with a camera at the image plane after the 4f, position 1 in Figure 3.2. The offset measured by the camera as the number of pixels is directly translated as displacement by converting the offset to mm. Secondly, to verify tip/tilt, we observe the Gaussian beam at the focal point with a camera, position 2 in Figure 3.2.

The offset measured in the far field was extracted from the CCD pixel array as an on-axis intensity measurement. Given an image I(x_i, y_i) where (x_i, y_i) are coordinates mapping each pixel. The measured offset and the focal length of the lens, L1, were used to calculate the tip/tilt angle [$\alpha = \arctan\left(\frac{\text{offset}}{\text{focal length}}\right)$]. The offset measured by the camera was determined by finding the difference between the two centre pixel positions of the Gaussian mode. One when there is no misalignment encoded on the SLM, (x_{co}, y_{co}) and the other when there is either tip/tilt or displacement encoded on the SLM, (x_c, y_c). The centre of the mass method was used to find the centre pixel position of the Gaussian beam on the image [71, 72]. This method involves using different intensities of each pixel on an image of the Gaussian beam to find the centre of mass of the Gaussian detected by the camera. In this way, the contribution of each pixel to the centre of the beam was weighted by its intensity value as expressed by

$$x = \frac{\sum_{i=0}^{M-1}\sum_{j=0}^{N-1} x_i \cdot I(x_i, y_j)}{\sum_{i=0}^{M-1}\sum_{j=0}^{N-1} I(x_i, y_j)} \tag{3.2a}$$

$$y = \frac{\sum_{i=0}^{M-1}\sum_{j=0}^{N-1} y_i \cdot I(x_i, y_j)}{\sum_{i=0}^{M-1}\sum_{j=0}^{N-1} I(x_i, y_j)} \tag{3.2b}$$

where the centroid position in the image is named (x_c, y_c), M and N are the pixel number in the x- and y-direction of the associated image, respectively. $I(x_i, y_j)$ is the intensity at the given coordinate (x_i, y_j).

The algorithm used to measure the beam's centre pixel position following Equation (3.2) is shown in Algo. 1. The initial centroid of the beam was determined using Algo. 1 when there is no tip/tilt and lateral displacement imposed for both cameras 1 and 2 in Figure 3.1. Then, the new beam centroid was determined using the same algorithm when either tip/tilt or lateral displacement was imposed on the SLM. The difference between the initial and the new beam centroid was used to calculate the tip/tilt on camera two and measure lateral displacement on camera 1.

Algorithm 1 :Calculation of beam center pixel position from an image

Require: im ▷ Input image
Ensure: $centerOfmass$ ▷ Center of mass coordinates
  Check dimension of im
  if ¬ isMatrix(im) **then**
    Error('Input image is expected to be bidimensional.')
  end if
  $im \leftarrow \text{double}(im)$
  $Itotal \leftarrow \sum_{i,j} im(i,j)$
  $a, b \leftarrow \text{size}(im)$
  $x \leftarrow 1 : b$
  $x \leftarrow x(ones(1,a),:)$
  $aux \leftarrow im \cdot x$
  $x_c \leftarrow \frac{\sum_{i,j} aux(i,j)}{Itotal}$
  $y \leftarrow 1 : a$
  $y \leftarrow y(ones(1,b),:)'$
  $aux \leftarrow im \cdot y$
  $y_c \leftarrow \frac{\sum_{i,j} aux(i,j)}{Itotal}$
  $centerOfmass \leftarrow [x_c, y_c]$
  Return $centerOfmass$

3.3 Validation of Dataset

3.3.1 Comparison of Measured and Simulated OAM Spectra

We first characterised OAM crosstalk using tip/tilt and displacement only. OAM spectra were measured for 3 cases: tip/tilt only, displacement only, and a combination of both. For the comparison of measured and simulated OAM spectra, we considered how they compared with each other and the existing theory of OAM crosstalk due to tip/tilt and lateral displacement. Figures 3.3 to 3.5 shows the OAM spectra of the Gaussian mode ($\ell_{\text{input}} = 0$)

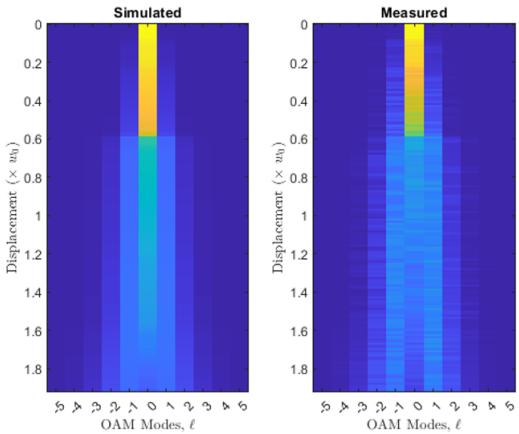

Figure 3.3: Measurement of OAM crosstalk ($\ell_{\text{input}} = 0$) with increasing displacement for the displacement-only case.

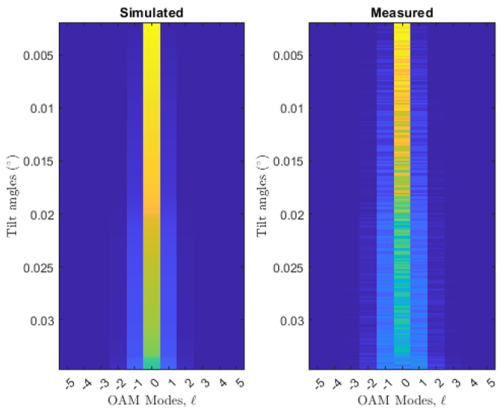

Figure 3.4: Measurement of OAM crosstalk ($\ell_{\text{input}} = 0$) with increasing tip/tilt for the tip/tilt only case.

for increasing tip/tilt and/or lateral displacement in the 3 cases for the generated dataset. Figure 3.3 and 3.4 show the measured OAM spectra when only one misalignment is imposed into the setup. Figure 3.5 shows the measured OAM spectra for a combination of tip/tilt and displacement that were introduced in the setup. The plot on the left shows the spectra when considering increasing values of tip/tilt in the presence of displacement, and the other on the left is when considering increasing the magnitude of the displacement in the tip/tilt. The spectrum broadens with increased misalignment, either tip/tilt or displacement. For the case of a combination of tip/tilt and displacement, the spectrum decreases or increases with an increase in the combination of tip/tilt and displacement. When adjustments are isolated to either tip/tilt or displacement, variations in their magnitude along the x or y axes directly correlate with changes in the OAM spectrum - an increase or decrease in magnitude corresponds accordingly. However, in the case involving simultaneous adjustments in both tip/tilt and displacement, the resultant changes in the OAM spectrum are dependent not only upon the magnitude but also on the directional orientation of these adjustments. This behaviour agrees with the findings reported in Ref [41].

The measured experimentally and the simulated dataset were compared to observe how well they correlate. The Pearson correlation coefficient [73] evaluates the similarity between the simulated and measured OAM spectra for the same misalignments. The high Pearson correlation coefficients of 0.96 for cases involving tip/tilt and displacement only and 0.93 for the case of the combination of both indicate a strong correlation between the simulated and

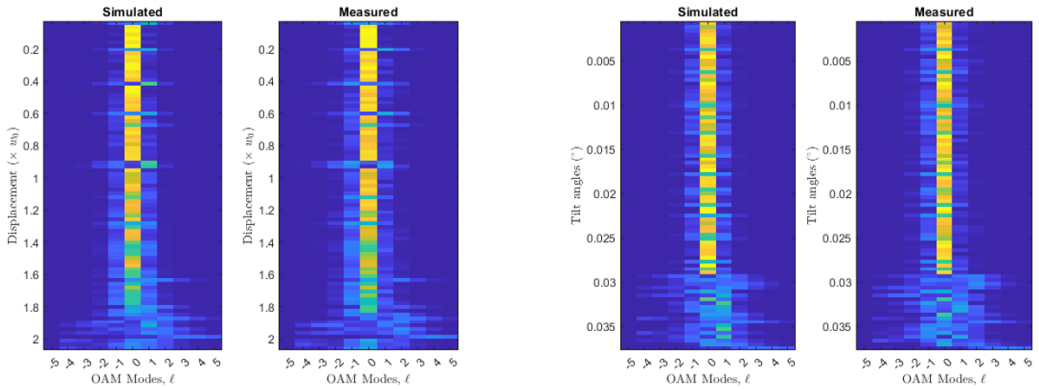

Figure 3.5: Measurement of OAM crosstalk ($\ell_{\text{input}} = 0$) with increasing tip/tilt and/or displacement for the case of a combination of both. OAM crosstalk measurement is shown when tip/tilt and displacement values imposed are considered separately.

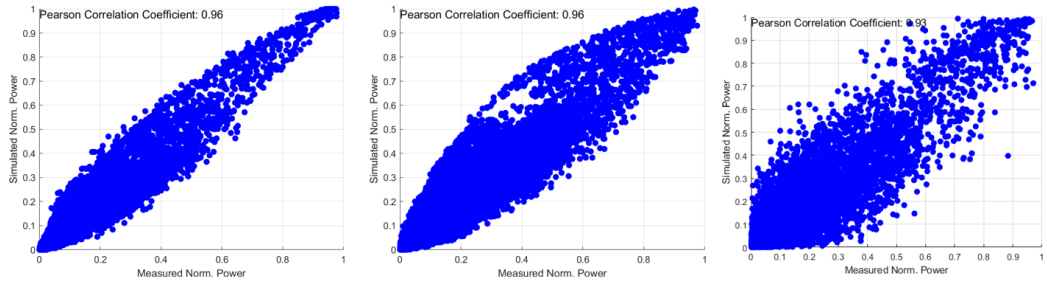

Figure 3.6: Correlation plots of simulated and (experimentally) measured normalised power with (a) tilt only, (b) lateral displacement only, and (c) a combination of both. High correlation coefficients: (a) 0.96, (b) 0.96, (c) 0.93, showing strong agreement in all cases.

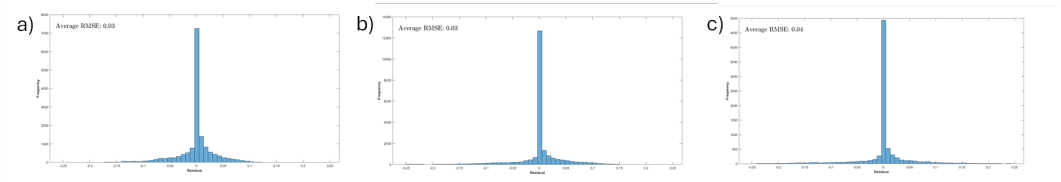

Figure 3.7: Residual plots showing three different cases with (a) tilt only, (b) lateral displacement only, and (c) a combination of both. The histogram of the residuals exhibits a random Gaussian characteristic shape. The RMSE value is slightly higher in the case of a combination of both.

measured OAM spectra. This suggests that the simulated spectra effectively capture the underlying dynamics of the system, producing results that closely resemble the experimentally measured spectra under various misalignment conditions. The correlation plots presented in Figure 3.6 visually demonstrate this strong correlation, with the normalised power values from modal decomposition aligning closely between the simulated and measured datasets. Figure 3.7 shows the mean RMSE errors of 0.038, 0.048, and 0.065, respectively, indicating the average discrepancies for cases involving tip/tilt only, displacement only and the combination of both. Notably, the cases of tip/tilt only and displacement only show similar errors, while the combined case exhibits a slightly higher error, nearly double. This discrepancy can be attributed to the linear relationship between changing either tip/tilt or displacement alone and the OAM spectra, which depend solely on magnitude. Conversely, the non-linear relationship between changing both tip/tilt and displacement simultaneously and the OAM

spectra, which rely on both magnitude and directional orientation, contributes to the higher error in the combined case.

A few random examples of the OAM spectra used to generate the correlation and residual plots are shown in Figures 3.8, 3.9, and 3.10. These examples depict the OAM spectra with their corresponding RMSE values for Gaussian mode and $\ell_{\text{input}} = \pm 3$, illustrating the impact of increasing values of tip/tilt and displacement for the three cases. The experimentally measured spectrum was taken as the ground truth. Figures 3.8 to 3.10 are cases of the tip/tilt only, displacement only, and a combination of both, respectively.

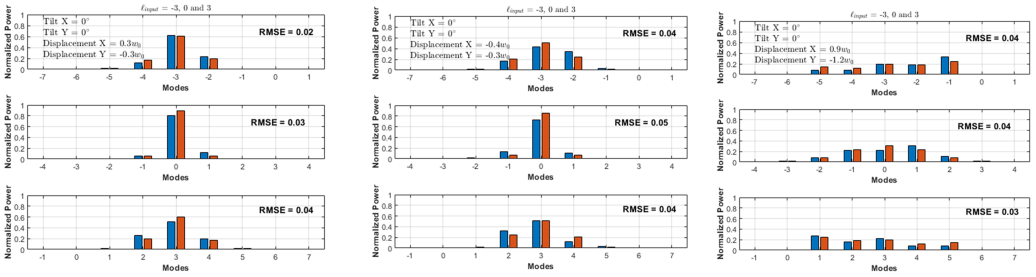

Figure 3.8: Model accuracy only shows several cases with lateral displacement. Blue bars are the ground truth modal decomposition; red bars are the simulated decomposition that will be used to train the NN. The input modes shown are ℓ_{input} = -3, 0 and 3 in the top, middle, and bottom rows, respectively, with increasing displacement magnitude.

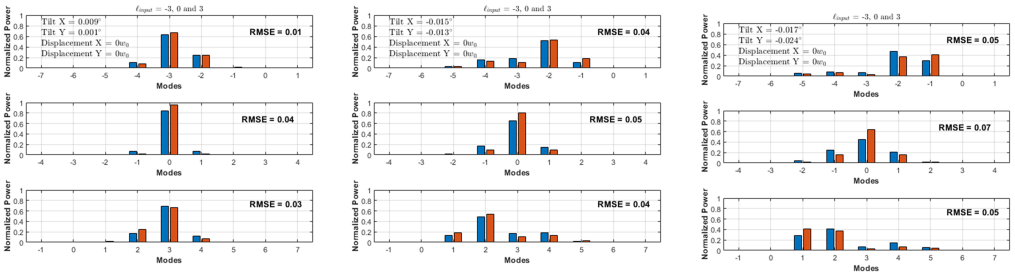

Figure 3.9: Model accuracy shows only several cases with tip/tilt. Blue bars are the ground truth modal decomposition; red bars are the simulated decomposition that will be used to train the NN. The input modes shown are ℓ_{input} = -3, 0 and 3 in the top, middle, and bottom rows, respectively, with increasing tip/tilt magnitude.

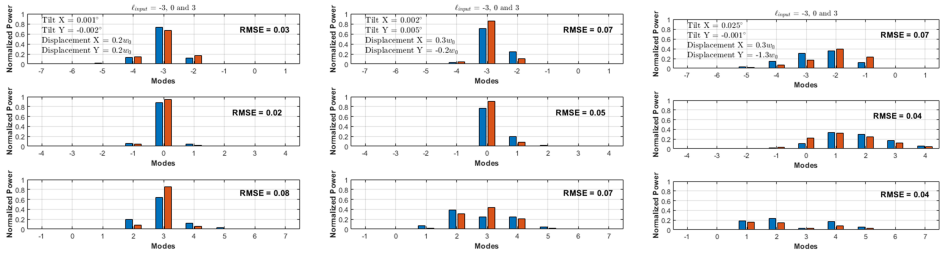

Figure 3.10: Model accuracy shows several cases with lateral displacement and tip/tilt. Blue bars are the ground truth modal decomposition; red bars are the simulated decomposition that will be used to train the NN. The input modes shown are ℓ_{input} = -3, 0 and 3 in the top, middle, and bottom rows, respectively, with increasing misalignment magnitude.

However, while these correlation coefficients show a high correlation between the simulated and measured spectra, they do not align perfectly. The experimentally measured spectra were conducted under similar laboratory conditions to those in the simulation, making them the standard against which the results must be judged. The residual distribution plots generated based on the normalised power values for cases involving tip/tilt only, displacement only, and a combination of both on input modes, ℓ_{input} = [-5,5] provide a visual representation of the discrepancies between the simulated and measured values. The residual plots exhibit Gaussian distribution, implying a consistent and reliably characterised error distribution across the dataset. The difference between the measured and the simulated spectra arises from slight misalignment in the setup and the fact that the SLM suffers from an inherent imperfection, which affects the amplitude and the phase of the modes and, therefore, causes inherent crosstalk within the system. These imperfections are not included in the simulation but were present in the spectra measured experimentally.

3.3.2 Verification of Lateral Displacement and Tip/Tilt

While the Pearson correlation coefficient and the residual distribution provided helpful information about the similarity between simulated and measured data, verifying the method used to impose the misalignment was also considered. The mean RMSE of the displacement-only scenario appears relatively more minor than that of the tip/tilt-only scenario. This subtle variance begs the question: what factors contribute to this discrepancy, especially considering that displacement and tip/tilt exert similar effects on the OAM spectrum when considered individually? Experimental verification of the tip/tilt and displacement measurements was conducted. Various tip/tilt and displacement values were encoded onto the hologram alongside a Gaussian mode. Equation (3.1) and misalignment measured from resulting values using the camera were used for the hologram creation. This process was repeated for the three scenarios: tip/tilt-only, displacement-only, and the case of a combination of both.

Figure 3.11 depicts the verified measurements of tip/tilt and displacement. Figure 3.11a illustrates the displacement measurements, revealing minimal variance between the encoded and measured displacement values. This variance remains consistent even when tip/tilt is simultaneously encoded with displacement. The line of best fit indicates a slight deviation of measured displacements from the encoded values for displacement values exceeding $1.5\omega_0$.

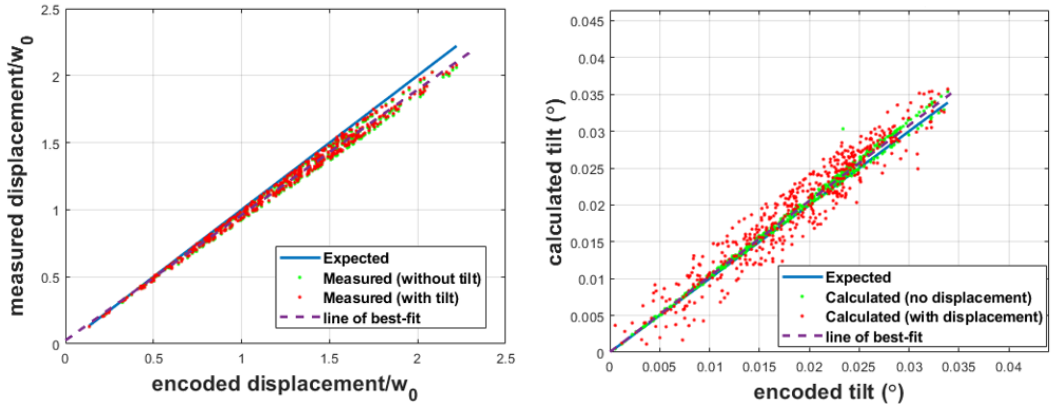

(a) Displacement measurements.

(b) Tip/Tilt measurements.

Figure 3.11: Plots showing the experimentally verified measurements of tip/tilt and lateral displacement in orange and green - the discrepancy is due to slight misalignments in the setup.

When no displacement is encoded, the tip/tilt measurements exhibit a similarly slight variance as shown in Figure 3.11b.

However, this variance increases when displacement is combined with tip/tilt encoding. We attribute this variance increase to slight misalignments in the setup and the inherently smaller magnitudes of tip/tilt measurements compared to displacement. As a result, tip/tilt measurements are particularly sensitive to even slight misalignments in the setup, which can increase the likelihood of errors. To address these misalignment issues, no static or adaptive correction methods were employed. Instead, we relied on trial-and-error adjustments of optical elements, such as focal point positions and camera settings, guided by the crosstalk matrix, to minimize these alignment challenges.

3.4 Summary

This chapter generated and validated OAM crosstalk induced by tip/tilt and displacement measurements, crucial for training a neural network in Chapter 4 due to the absence of an open-source dataset with similar measurements. Existing methods for characterising crosstalk, such as analytical expressions, were reviewed. The methodology details experimental setups for generating experimental and simulated datasets, with simulations used for dataset creation and experiments for verification. Verification was implemented to encode the SLM and measure tip/tilt and displacement values. The results demonstrate a strong correlation between measured and simulated OAM spectra, with Pearson correlation coefficients indicating a close match. Residual distribution plots reveal discrepancies due to setup imperfections and SLM errors. Mean RMSE values show average deviations, slightly higher for combined tip/tilt and displacement inputs. In this chapter, a dataset for training the neural network model in the next chapter was generated and verified.

CHAPTER 4

A Neural Network Model for OAM Crosstalk with Tilt and Displacement

RECENTLY, research has used CNN to examine the mode content of both free-space and fibre lasers using intensity images. The studies that employed CNN were primarily able to obtain both the amplitude and phase coefficients of OAM modes with successful results [**Sugawara2021ModalGrey-wolf-optimiser**, 74–76]. This often necessitated training complex neural network architectures on large datasets of interference patterns, which incurred significant computational costs. Other studies that did not use CNN used tabular data or images, and the use of diffraction gratings was common and could only obtain the amplitude coefficients [77, 78]. While these approaches yielded valuable insights, they were often impractical for real-world deployment due to their computational complexity and resource requirements.

Unlike prior works focusing on modal decomposition with neural networks using interference patterns or diffraction gratings, our work addresses the challenge of modelling decomposition with tip/tilt and displacement using neural networks. While most studies use image-based modal decomposition, we opt for tabular data. This choice is advantageous, especially in real-world telecommunications systems, where tabular data parameters such as lateral displacement and tip/tilt can be obtained using simple detectors such as a camera.

Some studies have provided analytical expression of OAM crosstalk caused by lateral displacement, tip/tilt, and OAM crosstalk [40, 41]. However, these traditional models can be cumbersome to apply and difficult to analyze in real-time at higher resolutions. Given the existing work on estimating future beam wander using neural networks [79] and analytical expression for OAM crosstalk, is it plausible to extend such models to estimate the OAM spectrum due to tip/tilt and displacement? In this chapter, we develop and verify a simple neural network model to estimate OAM crosstalk due to displacement and tip/tilt. The dataset used was generated in Chapter 3.

4.1 Model Development and Methodology

The approach to developing the neural network to model OAM crosstalk is outlined in this section. It consists of the following four steps: data pre-processing, model training, training and evaluation, and interpretation of results. Figure 4.1 shows a workflow diagram illustrating how the model was obtained, how this chapter connects with the previous

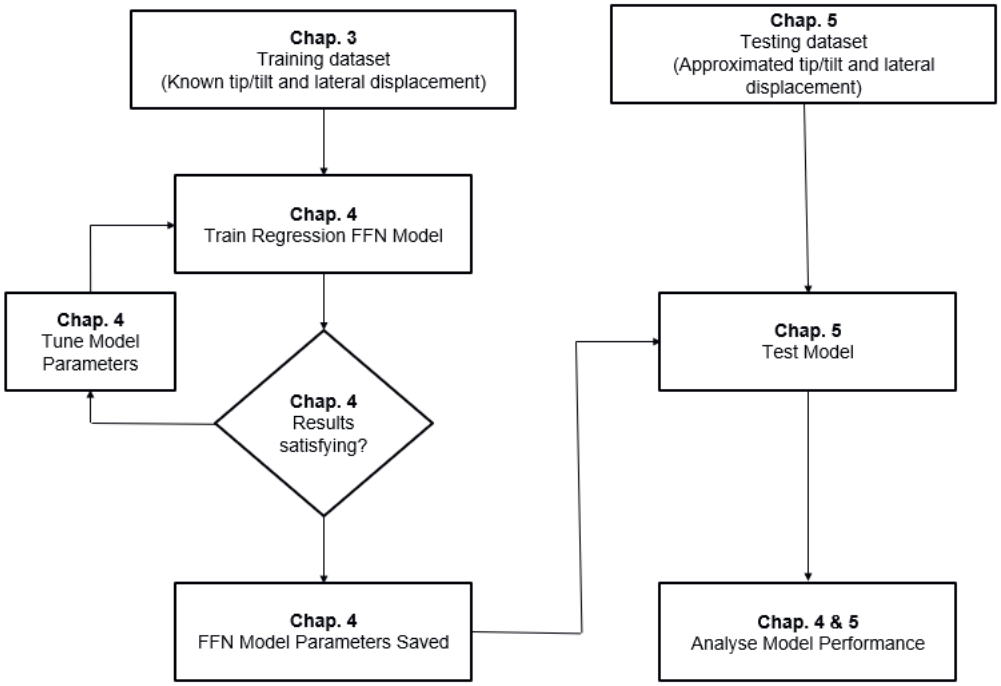

Figure 4.1: A methodology overview of the OAM crosstalk modelling using a simple neural network. The illustration shows the neural network development process and how it is linked to Chapter 3 and Chapter 5.

and subsequent chapters, and where each component is found in the document. We will investigate the impact of hyperparameters on the performance of the model.

4.2 Architecture

Figure 4.2 illustrates a typical FFNN architecture, consisting of an input layer followed by a repeating series of hidden layers and an output layer representing the normalised power values of the OAM spectrum of ℓ_{input}. Each layer is described in more detail below.

4.2.1 Input and Output Pre-processing

As stated in Section 3, we used the simulation dataset validated with the experimentally measured dataset as the input and output to the NN. The dataset consists of the input transmitted mode, ℓ_{input}, tip/tilt and displacement values as the input to the neural network, and their corresponding normalised power values of the OAM spectra as the output to the neural network. These features were chosen because tip/tilt and displacement have been shown to cause OAM crosstalk to a transmitted OAM mode [41]. The ranges of the input parameters and output values are as follows

1. tip/tilt (continuous values): [-0.25°, 0.25°]
2. lateral displacement (continuous values): [-1.5ω_0,1.5ω_0], where ω_0 =0.34 mm
3. ℓ_{input} (discrete values): [-5,5]
4. normalised power values (continuous values): [0,1]

The discrepancies in ranges and units among input variables present significant challenges. For instance, tip/tilt, measured in degrees and ranging from -0.25 to 0.25, and displacement, measured in factors of the beam waist (mm) and spanning from -1.5 to 1.5, require careful handling. Additionally, the representation of ℓ as having an inherent order or hierarchy disagrees with the nature of OAM modes, where each ℓ value denotes an independent and equally valid mode with its OAM spectrum. To address these complexities, z-score normalization is employed to standardise input features to have a mean of 0 and a standard deviation of 1 given by

$$z = \frac{x - \mu}{\sigma} \tag{4.1}$$

where z is the z-score which is the new mapping of the x, x is the tip/tilt or displacement in one particular direction (i.e. x or y direction), μ is the mean of the distribution, and σ is the standard deviation of the distribution. This technique reduces disparities in scale and magnitude, ensuring consistent scaling. Moreover, one-hot encoding preserves the categorical nature of OAM modes, ℓ, avoiding biased modelling based on magnitude, and aids in more accurate data representation and interpretation by the neural network. The output values are normalised power values; no further pre-processing was performed on them.

4.2.2 Input Layer

Tip/tilt and displacement values had two directions considered, the x and y directions, resulting in a sum of 4 features. The one-hot encoding of the 11 OAM modes resulted in 11 categories. Each category was represented by a vector of length 11, where only one element was hot. The total number of all input features is 15. The input vector had the dimensions of $I \in \mathbb{R}^{N\times 15}$, with an arbitrary number of rows representing the sample and a fixed number of 15 columns representing the features. No computational processing takes place in this layer, and it does not contain any trainable parameters.

4.2.3 Hidden Layer Layer

FFNN was chosen to model OAM crosstalk from tip/tilt and displacement due to its ability to handle complex mathematical computations. The hidden layer consists of neurons, each with its own set of weights and biases. The weights represent the connection strength between the input and the neuron, while the bias allows the neuron to shift its activation. Neurons compute a weighted sum of inputs, add bias, and pass it through an activation function, introducing non-linearity that allows it to learn complex patterns in the data. These trainable parameters (weights and biases) are adjusted during training to minimise the difference between estimated and actual outputs, defining the network's behaviour.

4.2.4 Output Layer

During the modal decomposition, 11 basis modes represent the OAM spectrum for each ℓ. The weights of all the basis modes were normalised, resulting in the normalised power values representing the OAM spectrum. For each input mode, ℓ_{input}, the basis modes considered for the spectra were the five adjacent modes on the left side of ℓ_{input}, five adjacent modes on the right side of ℓ_{input} and ℓ_{input} itself. Therefore, the output neurons represented the ten adjacent basis modes and the input modes. For any input mode, ℓ_{input}, the range of the 11 basis modes considered for its decomposition is below:

$$\triangle\ell = \ell_{\text{input}} \pm 5 \tag{4.2}$$

The output vector had the dimensions of $O \in \mathbb{R}^{N\times 11}$, with an arbitrary number of rows representing the sample and a fixed number of 11 columns representing the corresponding

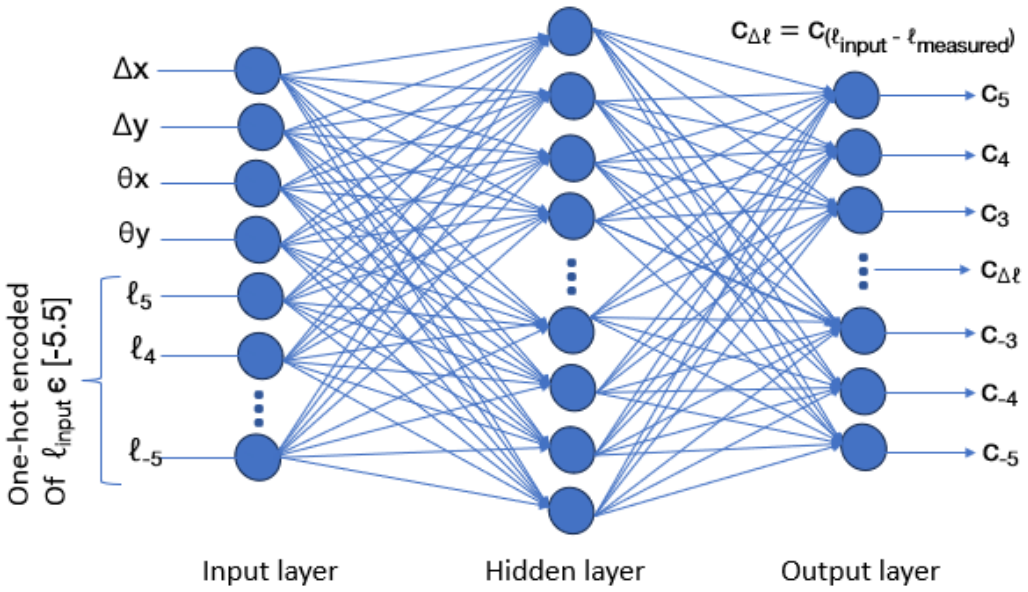

Figure 4.2: Architecture of the neural network structure with dimensions of 15 inputs and 11 outputs. The input nodes consists of displacement and tip/tilt and representation of $\ell_{\text{input}} \in$ [-5, 5]. The output nodes represent the normalised in the basis modes adjacent to the input mode, ℓ_{input} i.e OAM spectra.

normalised power values of the OAM spectrum of ℓ_{input}. The output layer has a linear activation function, allowing the model to output absolute power values without direct transformation. We applied a softmax to the raw outputs. The softmax is used as

$$\text{softmax}(O_{ij}) = \frac{e^{O_{ij}}}{\sum_{k=1}^{11} e^{O_{ik}}} \tag{4.3}$$

where O_{ij} is the raw output for the jth element (column) in the ith row of the output vector.

4.3 Training Process

We conducted experiments and ran models in the environment provided by the Google Colab notebook server (Python version 3.8.5 and Pytorch). During training, the aim is to minimise the model's loss function to achieve the best results. We first built the architecture using a manual search for hyperparameter tuning, while the second architecture resulted from hyperparameter tuning based on grid search. The first manual hyperparameter tuning was done by hand, which facilitated determining which hyperparameters to optimise and within which search space. The regression loss functions, activation functions, optimisers, the split ratio, and the number of hidden layers were tuned manually. The regression loss functions considered are MSE, MAE, and RMSE. The activation functions that were used are ReLu and Sigmoid. The optimisers considered were SGD, Adadelta, Adagrad, RMSSprop, and Adam. The loss functions, optimisers, and activation functions were changed, and the average loss was monitored for comparison. The split ratio of the training and the validation dataset was altered between 60/40, 70/30, and 80/20. The epoch was set to 250, and the learning rate was set to 0.001. We began with a single hidden layer with two neurons and iteratively changed the number of neurons and layers to find the optimal structure. We found that a network with two hidden layers, each with 32 neurons, provides

the best results with the smallest network size, and it was chosen as the final structure. The MAE loss function for training and validation monotonically decreased with training epochs, confirming that data was not overfitted despite the fluctuations, which are inevitable consequences of the stochastic approach of mini-batch gradient descent in Adam (batch size = 32). The architecture with the lowest validation loss was picked for modelling OAM crosstalk.

Secondly, we optimised the model's hyperparameters using grid search. The fine-tuned hyperparameters are the learning rate, the number of neurons in the hidden layer, the number of hidden layers, and batch size. From the observations made from the manual tuning, the dataset was randomly shuffled and split into training and validation with a splitting ratio of 70/30. The sigmoid activation function was used for all the layers except the output layer. MSE loss was used as the loss function, and the Adam algorithm was used as the optimiser. The final model network architecture was obtained from the best hyperparameters from the grid search.

4.4 Performance Metrics

In this section, we introduce the evaluation metrics used to assess the behaviour of learned models when applied to a dataset of size, N and thereby assess the multi-output regression approach used for modelling OAM crosstalk. Let the simulated normalised power values be $y = \{y_1, y_2, \ldots, y_n\}$ and model's estimated normalised power values $\hat{y} = \{\hat{y}_1, \hat{y}_2, \ldots, \hat{y}_n\}$. The four evaluation metrics used to assess multi-output regression models are

1. **MSE:**
$$\text{MSE} = \frac{1}{N}\sum_{i=1}^{N}(y_i - \hat{y}_i)^2 \tag{4.4}$$

2. **RMSE:**
$$\text{RMSE} = \sqrt{\frac{1}{N}\sum_{i=1}^{N}(y_i - \hat{y}_i)^2} \tag{4.5}$$

3. **Coefficient of Determination (R^2)**:
$$R^2 = 1 - \frac{\sum_{i=1}^{N}(y_i - \hat{y}_i)^2}{\sum_{i=1}^{N}(y_i - \bar{y})^2} \tag{4.6}$$

4. **Residual**:
$$\text{Residual} = y_i - \hat{y}_i \tag{4.7}$$

The model's performance was assessed using RMSE (Equation (4.5)). RMSE is a modified version of MSE in Equation (4.4) that normalises the units of MSE. MSE was the model's loss function. Both metrics range from [0, +∞). When the simulated normalised power matches the model's normalised power, the evaluation metric is zero, indicating optimal model performance. However, as the error between simulated and model normalised power increases, so does the evaluation metric. Since these metrics range from zero to +∞, a single value does not fully describe the model's performance concerning the distribution of normalised power values (i.e. OAM spectra). R^2 in Equation (4.6) gives a high score when the majority of simulated normalised power values match the model, but it's capped at one or 100% for a perfect fit [80]. R^2 is a valuable metric for evaluating model fit. Using residual plots/histograms from Equation (4.7) provides insight into the model's performance and potential bias in the estimates. The neural network has a multi-output, implying that the metrics above will be averaged.

4.5 Results and Discussion

4.5.1 Correlation of the Model on the 3 Cases

The dataset generated with the simulation and verified with the experiment was used to train the model. The dataset was split into training and validation using a 70:30 ratio. The model was trained and validated using the dataset that contained the measurements with the 3 cases of displacement only, tip/tilt only, and finally, a combination of both. The model takes tip/tilt, displacement, and the ℓ_{input} values as inputs to estimate the corresponding OAM spectra given by the normalised power values of 11 modes as the output. Figure 4.3 to 4.5 graphically demonstrate the correlation plots for simulated (actual) and NN-estimated (outcome) normalised values for each of the 3 cases on the dataset showing the correlation of determination. The output normalised power values from the model are non-negative, within the expected range of $\in [0, 1]$ and sum up to one. This is because a softmax function is used at the end of the model's output. It can be observed that the cases of individual misalignments had a very high correlation shown with the R^2 of above 0.99, as well as the discrepancies between actual and NN-estimated normalised power values quantified by the absolute error of ± 0.04 shown by the corresponding residual histograms in Figure 4.3 and 4.4. Figure 4.5, the displacement and tip/tilt case had a slightly lower R^2 of 98%. The residual histogram of the case with both tip/tilt and displacement has an absolute error of ± 0.1, which is acceptable. The closeness of data points to regression lines indicates better estimations of the developed model. This shows how the model-estimated normalised power values agree with the simulated normalised power values. Low RMSE values of the normalised values of at least 0.01 indicate the same. For the 3 cases, the RMSE values of the validation data are slightly lower than that of the training data, indicating the model can generalise on unseen data. The residual plots for all three cases have a random Gaussian characteristic shape, implying that the residuals are Gaussian white noise and similar. In the case of a combination of tip/tilt and displacement, we can see that the error is almost double that of the individual cases. This difference can be seen in the slightly larger variance in the correlation plot of the case with both misalignments. This is because the relationship between the OAM spectrum is much more complex as it depends on both the magnitude and direction orientation of the misalignments, unlike in the case of individual misalignments that only rely on the magnitude [41]. These results indicate no input between the tip/tilt and displacement, which is significantly more important than the other.

4.5.2 Correlation of the Output Neurons

The variance of the case of a combination of tip/tilt and displacement is slightly more significant than that of the individual misalignment cases for lower normalised power values. Given the high R^2 values in the 3 cases and that the model is multi-output, are all output neurons in the output layer equally contributing to the high R^2 value, or are there specific outputs that are performing better than others leading to the high variance? Considering the whole dataset without grouping it into the 3 cases, we examined the correlation between the NN-estimated and the simulated normalised power values for each of the 11 neurons. Figure 4.6 shows the correlation plots for the 11 individual output neurons. One observation to note is that the average RMSE and R^2 values decrease as one moves from neuron$\triangle\ell = 0$ to $\triangle\ell = \pm 5$, where neuron $\triangle\ell = 0$ contains the normalised power value detected in the basis of ℓ_{input} mode that is part of the input. The other non-zero neuron $\triangle\ell$ contains the normalised power values corresponding to the adjacent basis modes to ℓ_{input}. These results show that the model can estimate the normalised power in the ℓ_{input} and the adjacent modes with a high correlation. However, in the adjacent modes such as neurons $\triangle\ell = \pm 4$ and ± 5, which are further away from the ℓ_{input} its performance drops slightly which is similar to the high variance shown in the case of a combination of tip/tilt and displacement. The results suggest that the accuracy of the model's estimation depends

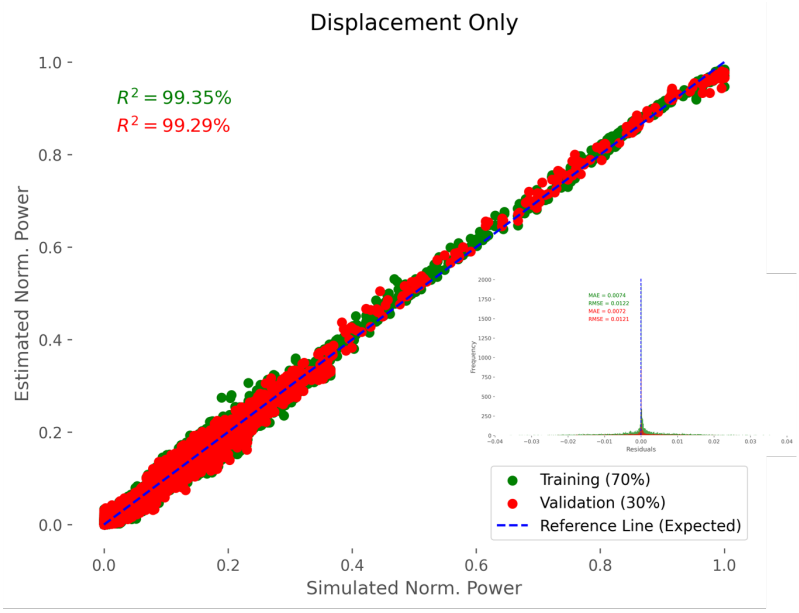

Figure 4.3: Correlation and residual histogram of normalised power for $\ell_{\text{input}} \in [-5, 5]$ between simulated and NN-estimated values when there is only displacement only. The correlation plot illustrates the relationship between the simulated and NN-estimated values, with a correlation of determination values of $R^2 = 99.29\%$, indicating a strong match. The residual histogram displays a Gaussian distribution of errors, showing the model's accuracy and good estimation of training and validation datasets.

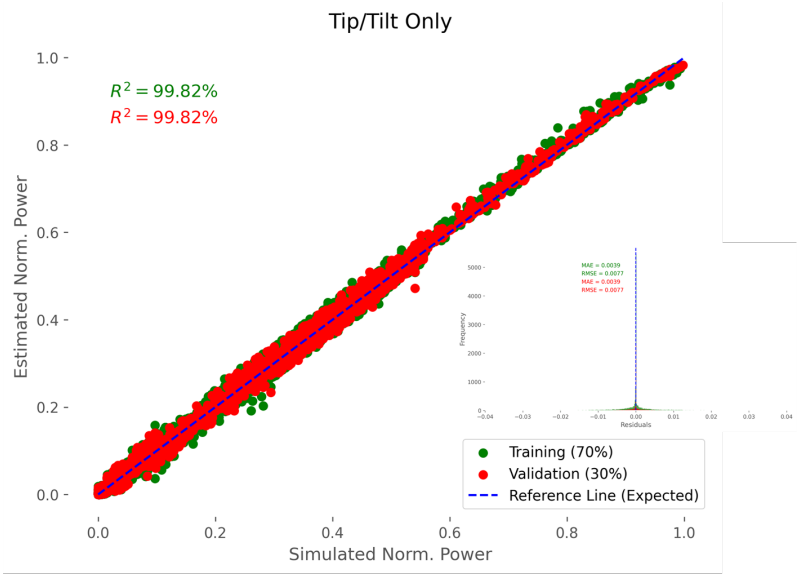

Figure 4.4: Correlation and residual histogram of normalised power for $\ell_{\text{input}} \in [-5, 5]$ between simulated and NN-estimated values when there is only tip/tilt only. The correlation plot illustrates the relationship between the simulated and NN-estimated values, with a correlation of determination values of $R^2 = 99.82\%$, indicating a strong match. The residual histogram displays a Gaussian distribution of errors, showing the model's accuracy and good estimation of training and validation datasets. The training and validation datasets were split with a ratio of 70:30.

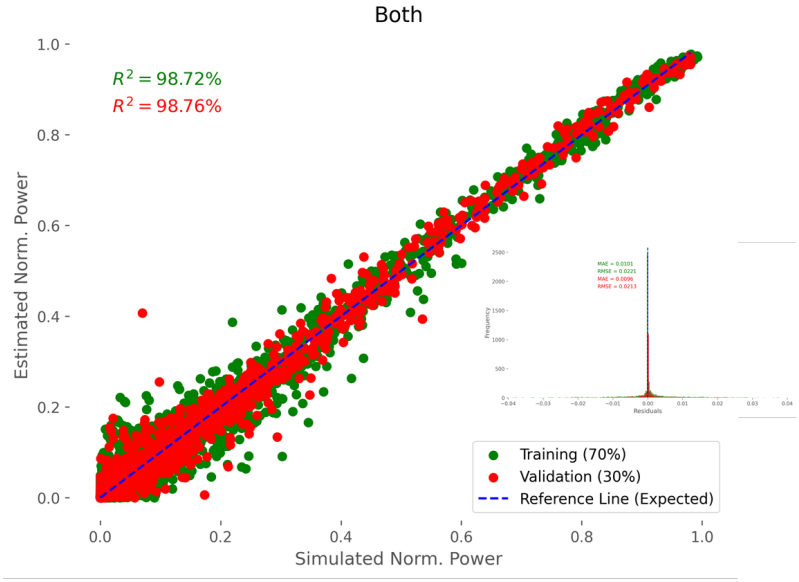

Figure 4.5: Correlation and residual histogram of normalised power for $\ell_{\text{input}} \in [-5, 5]$ between simulated and NN-estimated values for the case of the combination of tip/tilt and displacement. The correlation plot illustrates the relationship between the simulated and NN-estimated values, with a correlation of determination values of R^2 = 99.72%, indicating a strong match. The residual histogram displays a Gaussian distribution of errors, showing the model's accuracy and good estimation of training and validation datasets.

not only on the amount of the normalised power being estimated but also on the position away from the ℓ_{input}. This is likely because when modal decomposition, the more significant the number of basis modes being considered, the more accurate the measurements. The low RMSE in the neurons positioned far away from the $\triangle\ell = 0$ might suggest a slight discrepancy in magnitude between the model's output and the simulated normalised value. Still, they have very low validation R^2 values, suggesting a low correlation. Therefore, a low RMSE value indicates a good fit in disguise only because the values in these neurons are small in magnitude; hence, the discrepancy is slight. However, the low correlation in estimating the neurons far away from the centre neuron does not cause any serious concerns to our model because, in most cases, these far away neurons have normalised power values close to zero.

4.5.3 Measured, Simulated and NN-estimated Spectra

Some examples of the comparison of the measured (experimentally), simulated, and NN-estimated OAM spectra for the case of displacement only in Figure 4.7, tip/tilt only in Figure 4.8 and a combination of both in Figure 4.9. The simulated and estimated OAM spectra match well, showing how well the neural network can estimate OAM for all 3 cases, as seen by the similar behaviour of the spectra to various tip/tilt and displacement combinations. Although the agreement between the measured and simulated or estimated OAM spectra is close, the match is imperfect. This can be seen with relatively the same RMSE values for simulated and estimated OAM spectra in Figure 4.7 to 4.9. The difference between the measured and simulated spectra arises from slight misalignment in the setup as highlighted in Chapter 3, causing crosstalk within the system. The difference between the measured and estimated spectra comes from the simulated measurement used in training, and sometimes, there are additional crosstalk values as the network softmax function at the output layer keeps the sum of the network output to 1, which can be seen in the side-bands.

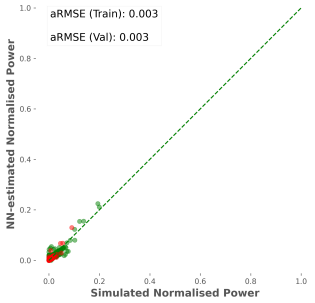

(a) $\Delta\ell = -5$, $R^2_{\text{train}} = 0.88$, $R^2_{\text{valid}} = 0.55$

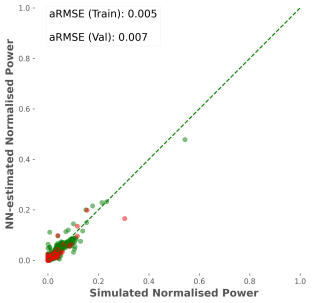

(b) $\Delta\ell = -4$, $R^2_{\text{train}} = 0.90$, $R^2_{\text{valid}} = 0.93$

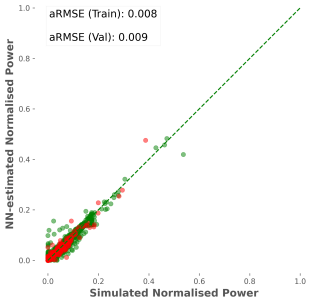

(c) $\Delta\ell = -3$, $R^2_{\text{train}} = 0.95$, $R^2_{\text{valid}} = 0.92$

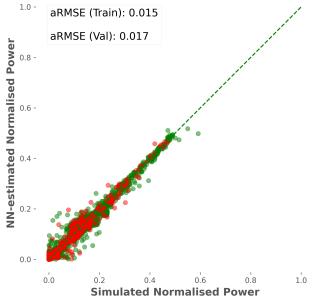

(d) $\Delta\ell = -2$, $R^2_{\text{train}} = 0.98$, $R^2_{\text{valid}} = 0.97$

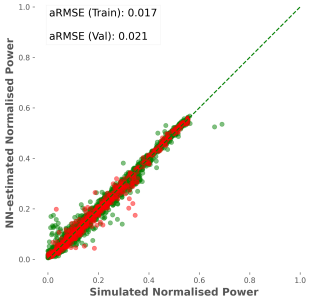

(e) $\Delta\ell = -1$, $R^2_{\text{train}} = 0.98$, $R^2_{\text{valid}} = 0.98$

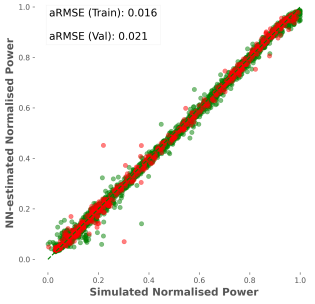

(f) $\Delta\ell = 0$, $R^2_{\text{train}} = 1$, $R^2_{\text{valid}} = 1$

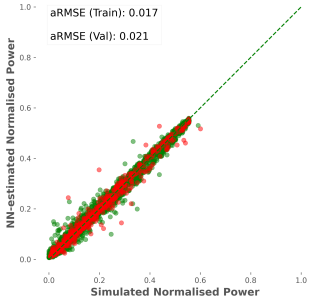

(g) $\Delta\ell = 1$, $R^2_{\text{train}} = 0.98$, $R^2_{\text{valid}} = 0.97$

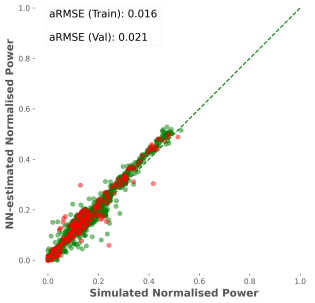

(h) $\Delta\ell = 2$, $R^2_{\text{train}} = 0.98$, $R^2_{\text{valid}} = 0.97$

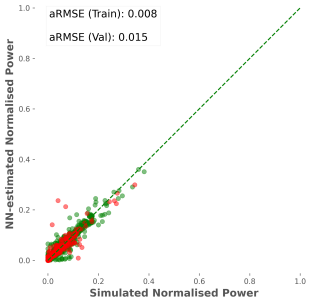

(i) $\Delta\ell = 3$, $R^2_{\text{train}} = 0.92$, $R^2_{\text{valid}} = 0.76$

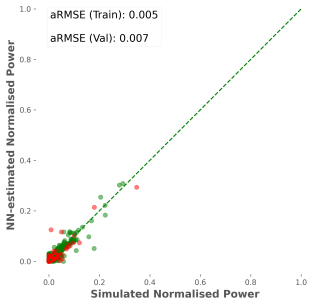

(j) $\Delta\ell = 4$, $R^2_{\text{train}} = 0.89$, $R^2_{\text{valid}} = 0.78$

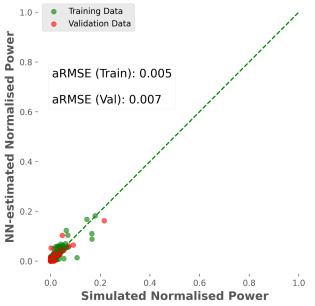

(k) $\Delta\ell = 5$, $R^2_{\text{train}} = 0.87$, $R^2_{\text{valid}} = 0.73$

Figure 4.6: Correlation analysis across 11 output nodes denoted by $\Delta\ell$. The subfigures show how the model's estimation matches actual values for different output neurons. Neuron $\Delta\ell$ = 0 corresponds to the input mode, while adjacent neurons represent neighbouring modes (crosstalk). The green and red dots denote training and validation normalised power values. The subplots showcase average RMSE and R^2 values on the training and validation dataset.

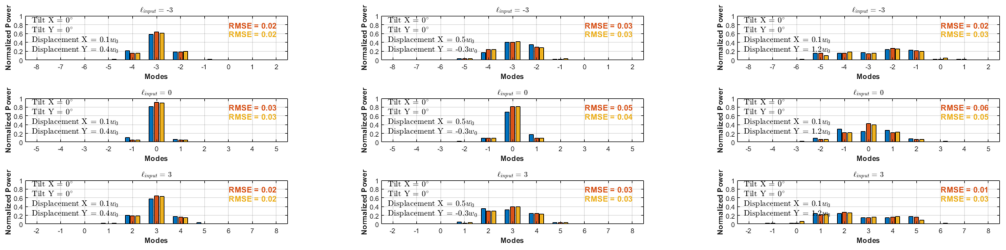

(a) Displacement only (0.1 ω_0, 0.4 ω_0) on ℓ_{input}= -3, 0 and 3. **(b)** Displacement only (0.5 ω_0, -0.3 ω_0) on ℓ_{input}= -3, 0 and 3. **(c)** Displacement only (0.1 ω_0, 1.2 ω_0) on ℓ_{input}= -3, 0 and 3.

Figure 4.7: Model accuracy is illustrated across the case with lateral displacement only. Blue bars: Experimentally measured normalised power values (Ground Truth); Red bars: Simulated normalised power (used for NN training); Orange bars: NN-estimated with the final model. Input modes: ℓ_{input} = -3, 0, and 3 in the top, middle, and bottom rows, respectively, with increasing displacement magnitude from Figure 4.7a to 4.7c.

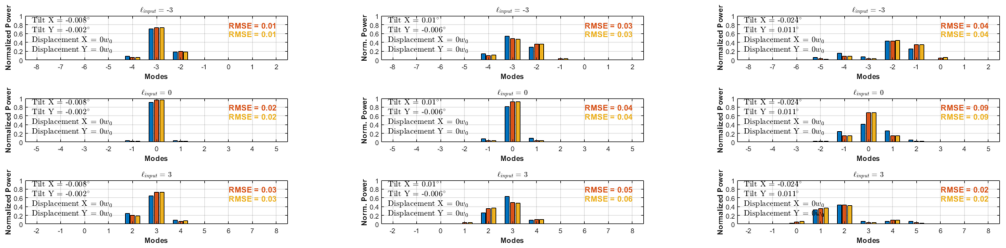

(a) Tip/tilt only $(-0.008°, 0.002°)$ on ℓ_{input}= -3, 0 and 3. **(b)** Tip/tilt only $(0.01°, -0.006°)$ on ℓ_{input}= -3, 0 and 3. **(c)** Tip/tilt only $(-0.024°, 0.011°)$ on ℓ_{input}= -3, 0 and 3.

Figure 4.8: Model accuracy is illustrated across the case with tip/tilt only. Blue bars: Experimentally measured normalised power values (Ground Truth); Red bars: Simulated normalised power (used for NN training); Orange bars: NN-estimated with the final model. Input modes: ℓ_{input} = -3, 0, and 3 in the top, middle, and bottom rows, respectively, with increasing tip/tilt magnitude from Figure 4.8a to 4.8c.

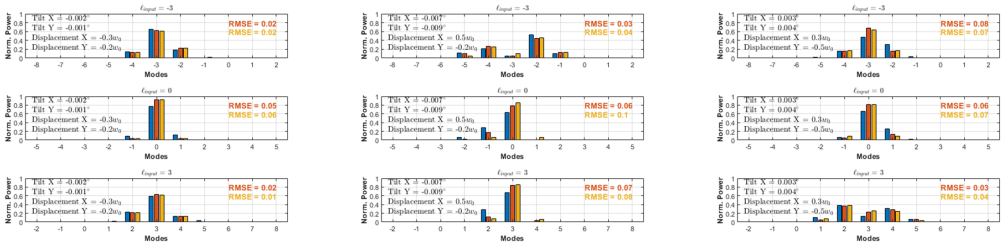

(a) Combined (-0.3ω_0, -0.2ω_0, $-0.002°, -0.001°$) on ℓ_{input}= -3, 0 and 3. **(b)** Combined (0.5ω_0, -0.9ω_0, $-0.007°, -0.009°$) on ℓ_{input}= -3, 0 and 3. **(c)** Tip/tilt only (0.3ω_0, -0.5ω_0, $0.003°, 0.004°$) on ℓ_{input}= -3, 0 and 3.

Figure 4.9: Model accuracy is illustrated across the case with lateral displacement and tip/tilt combined. Blue bars: Experimentally measured normalised power values (Ground Truth); Red bars: Simulated normalised power (used for NN training); Orange bars: NN-estimated with the final model. Input modes: ℓ_{input} = -3, 0, and 3 in the top, middle, and bottom rows, respectively, with increasing misalignment magnitude from Figure 4.9a to 4.9c.

Therefore, the high correlation of the simulated and the estimated normalised power and Gaussian-shaped residual histogram indicate that the developed network is a good fit for the measured OAM spectrum due to the 3 cases of known tip/tilt and displacement values in the x and y directions for input modes, ℓ_{input} between -5 to 5. The close agreement between estimated and simulated spectra highlights the model's ability to generalise the training data well. However, is the trained model still a good fit for the OAM spectrum due to atmospheric turbulence? How well does it fit the OAM spectrum in the presence of turbulence aberrations?

4.5.4 Hyperparameters optimisation

Hyperparameter optimisation was a pivotal step in refining the neural network's performance. In Figure 4.10a, the training and validation losses are illustrated for various regression loss functions, including MSE, MAE, and RMSE. This comparison allowed for selecting the most suitable loss function, with MSE demonstrating the lowest average loss. Furthermore, Figure 4.10b illustrates the impact of different optimisers on the average MSE loss. The tested optimisers were SGD, Adadelta, Adagrad, RMSProp, and Adam. The Adam optimiser was chosen as the optimal choice for optimisation because of the lowest validation loss. Figure 4.11 to 4.13 show the average MSE loss for 1, 2 and 3 hidden layers. Each figure shows the average MSE loss of increasing the number of neurons in a specific number of hidden layers. These loss curves were used to observe the model's sensitivity to hidden layer configurations, aiding in selecting an optimal architecture for the neural network. Figure 4.12 shows that when there are 64 neurons in each layer of a network with two hidden layers. However, the network with two hidden layers, each with 32 neurons, was chosen as the final network because the difference in the MSE loss is insignificant compared to the difference in the architecture, hence the model parameters to update.

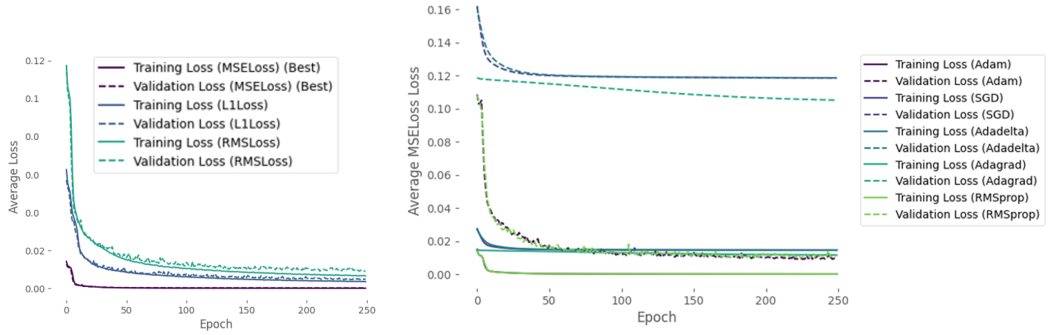

(a) Different regression loss functions.

(b) Different optimisers.

Figure 4.10: Comparing training and validation losses for different scenarios.

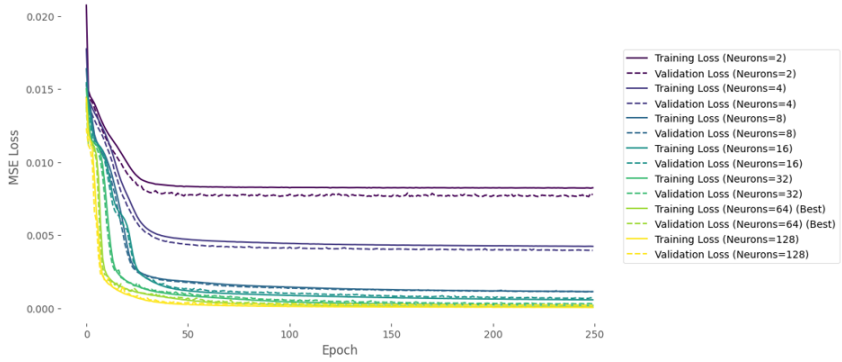

Figure 4.11: Training and validation losses for different neurons in 1 hidden layer. The average MSE loss is shown for an increasing number of neurons.

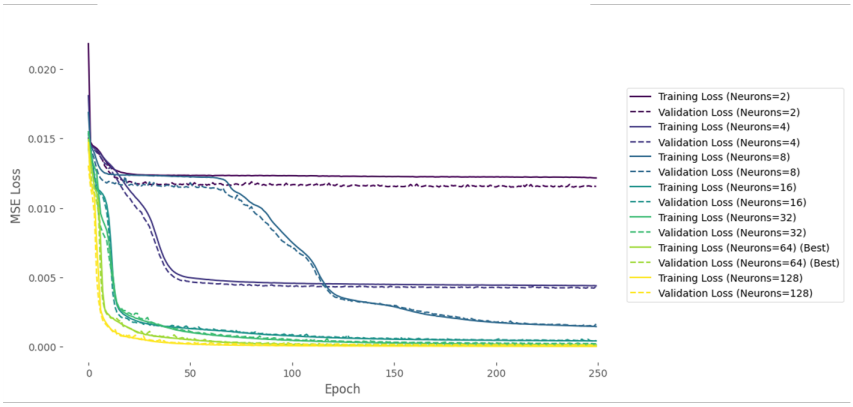

Figure 4.12: Training and validation losses for neurons in 2 hidden layers. The average MSE loss is shown for an increasing number of neurons.

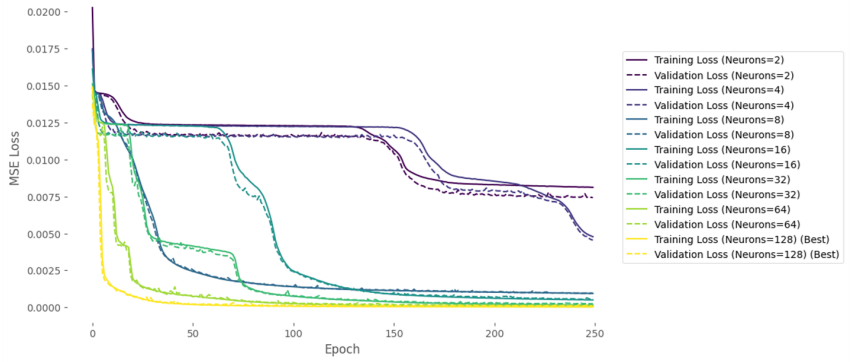

Figure 4.13: Training and validation losses for different neurons in 3 hidden layers. The average MSE loss is shown for an increasing number of neurons.

4.6 Conclusion

Atmospheric turbulence induces crosstalk in OAM modes, notably through lateral displacement and tip/tilt effects, impacting the performance of MDM systems. Analytical

models exist for OAM crosstalk caused by tip/tilt and displacement for Gaussian modes, while neural networks have proven effective in obtaining OAM coefficients. We developed and verified a simple neural network model for OAM crosstalk induced by tip/tilt and lateral displacement across ℓ_{input} modes in the range of [-5, 5]. Our findings show strong correlations between simulated and estimated normalised power values: individual misalignments (displacement or tip/tilt) had a high R^2 value and slightly lower for combined misalignments with an RMSE of a small on the normalised power values. This suggests a simple neural network can effectively generalise OAM spectra affected by tip/tilt and displacement.

CHAPTER 5

Accuracy of the Simplified Model in Turbulence

FOR long-distance MDM systems, achieving both reliability and high-speed transmission presents a big challenge, primarily due to crosstalk issues arising from atmospheric turbulence. Atmospheric turbulence causes beam spreading, scintillation and beam wander, which can be reduced with Adaptive Optics (AO) systems. However, this system's implementation can be costly [81]. Digital solutions like optimised error correction or signal processing offer more economical alternatives. Among the leading causes behind crosstalk errors in MDM systems, lateral displacement and tip/tilt at the receiver are the major effects [40, 41, 55]. Ref [43] suggested beam wander/angle of arrival estimation for forecasting OAM crosstalk can greatly improve communication system reliability [43, 82]. Firstly, developing an OAM crosstalk neural network model enables the estimation of future OAM crosstalk, enhancing system performance regarding bit error rate [83].

Given that there have been neural network models for estimating beam wander [79] and atmospheric turbulence phase [84] for MDM systems. The majority of turbulence is predominantly tip/tilt over 86% of the mean-square phase value [18, 42], leading to subsequent displacement during propagation, could the simple model developed in Chapter 4 serve as a form of "compressive sensing" approach? This can seen as simplifying OAM beams in atmospheric turbulence, which is a random complicated system with several effects on the beam, to OAM beams in tip/tilt and lateral displacement because tip/tilt is one of the main aberrations of turbulence [18] since the simple neural network model from the previous chapter was trained on $\approx 86\%$ of the effects of turbulence, specifically lateral displacement and tilt. However, turbulence encompasses a broader range of effects beyond displacement and tilt. The remaining $\approx 14\%$ of the other aberrations, such as astigmatism, are unknown to the model. *Can the simple neural network generalise its estimations on approximated measurements in the presence of additional aberrations without retraining it?*

In this chapter, we examine the accuracy of the simple trained neural network model from Chapter 4 using new tip/tilt and displacement values approximated in the presence of other effects of turbulence as the testing dataset. The testing dataset of the approximated tip/tilt and displacement is generated based on the centroid of the received beam. It covers a similar range of values to those on which the neural network was trained so that there is a fair idea of how well it performs. We then apply the trained model to this testing dataset to assess its accuracy in estimating OAM crosstalk under turbulent conditions. We show that

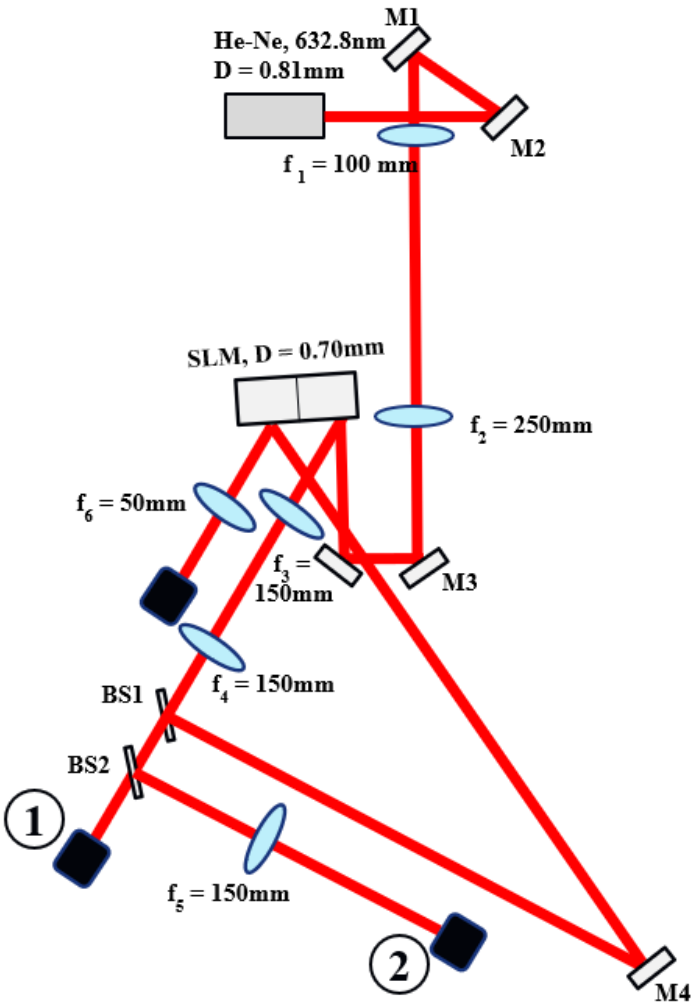

Figure 5.1: The setup simulates turbulence using Zernike polynomials.

the simple neural network trained only on tilt and displacement can give good results in the presence of other turbulence aberrations.

This study not only contributes to the understanding of OAM beam behaviour in turbulence but also facilitates the creation of optimised (and possibly less computationally intensive) schemes to correct errors due to crosstalk in both MDM and modal diversity, perhaps estimating the temporal evolution of OAM crosstalk in turbulence.

5.1 Experimental Setup and Methodology

The setup shown in Figure 5.1 was used to simulate turbulence using a phase screen added to the mode on the SLM, and the OAM spectrum of the final field was measured as before with the modal decomposition method. Cameras 1 and 2 were used to approximate displacement and tip/tilt, respectively. This setup looks similar to the setup shown earlier in Figure 3.1 in Chapter 3 used to characterise OAM crosstalk due to tip/tilt and displacement. The main difference comes from the fact that the generation of the testing dataset involves turbulence, which is not tilt/tip and displacement only but is other higher-order aberrations. Therefore,

the hologram encoded on the SLM has to be different. The hologram encoded in Figure 5.1 has a pure mode and a phase screen for the simulated turbulence.

5.1.1 Simulating Turbulence with Zernike polynomials

Following the Noll method, the turbulence phase screen was generated using a direct superposition of Zernike polynomials and then encoded onto the mode hologram. This involved superposing Zernike polynomials according to the expansion by

$$\phi(x,y) = \sum_{j=0} a_j Z_j(x,y) \equiv \sum_{j=0} a_j Z_j(r,\theta) \tag{5.1}$$

where $\phi(x,y)$ represents the wavefront to be described, a_j are the coefficients determining the weights of each Zernike polynomial $Z_j(r,\theta)$, or equivalently $Z_{m,n}(r,\theta)$, in the expansion and j is an index running from 0 to some maximum value, indicating the Zernike mode being considered.

Zernike polynomials form a series of orthogonal polynomials defined over a unit circle, frequently employed to characterise wavefront distortions in optical beams [85]. These polynomials are expressed as

$$Z_n^m(r,\theta) = \begin{cases} R_n^m(r)\cos(m\theta), & \text{for } m \geq 0 \\ R_n^m(r)\sin(m\theta), & \text{for } m < 0 \end{cases}. \tag{5.2}$$

where n is a non-negative integer, called the radial order. m is an integer with $|m| \leq n$ and determines the azimuthal frequency. ρ is the radial coordinate, and θ is the azimuthal angle. This expression holds when the indices m and n meet the conditions $m \leq n$ as per the Noll method [42] and $n - |m|$ is even. In this context, r is constrained to lie within a unit circle, while θ is measured clockwise from the positive y-axis. Table 5.1 shows a few examples of the Zernike terms, including tip/tilt and their corresponding indices. The radial function R_n^m can be written as

$$R_n^m(\rho) = \sum_{k=0}^{(n-m)/2} (-1)^k \frac{(n-k)!}{k! \cdot \left(\frac{n+m}{2}-k\right)! \cdot \left(\frac{n-m}{2}-k\right)!} \rho^{n-2k} \tag{5.3}$$

where k is a non-negative integer used as an index in the summation. n is the radial order of the Zernike polynomial. m is the azimuthal order of the Zernike polynomial. ρ is the radial coordinate in the unit circle.

The coefficients a_j can be drawn from a normal distribution characterised by a zero mean and a variance denoted by

$$\sigma_{nm}^2 = I_{nm} \left(\frac{D}{r_0}\right)^{5/3} \tag{5.4}$$

The values of I_{mn} are obtained from the diagonal terms of the Noll matrix [42] given by

$$I_{nm} = \frac{0.15337(-1)^{n-m}(n+1)\Gamma(14/3)\Gamma(n-5/6)}{\Gamma(17/6)^2\Gamma(n+23/6)} \tag{5.5}$$

Consequently, the phase screens are created by generating random samples from a normal distribution with a suitable variance for each coefficient. These coefficients are then utilised in the summation of Equation (5.1) to generate a phase function that accurately represents turbulence. Each sampling from the random distribution results in new coefficients, generating a new phase screen. Running these phase screens simulates varying turbulence of consistent strength, adhering to the Kolmogorov statistics [42].

Table 5.1: A few selected Zernike polynomials terms mapped to well-known wavefront aberrations.

(n,m)	**Abberation**
(0,0)	Piston
(1,-1), (1,1)	Tip and Tilt
(2,-2), (2, 2)	Astigmatism
(2, 0)	Defocus
(3, -3), (3, 3)	Trefoil
(3, -1), (3, 1)	Coma
(4, 0)	Spherical

The phase screens were verified to ensure that their turbulence strength is consistent with the programmed value of D/r_0. For verification, the Strehl Ratio (SR) provided a convenient relationship between measured intensities and turbulence strength D/r_0. In the presence of simulated turbulence, the encoded mode on the SLM changes from Equation (3.1) that has tip/tilt and displacement only to become

$$U(x,y) = U^{LG}(x,y) \exp\left(i \sum_j a_j Z_j(x,y)\right) \tag{5.6}$$

For each input OAM mode, modal decomposition was performed for 100 random turbulence screens for each Strehl Ratio from 1.0 (no turbulence) to 0.1 (strong turbulence). The corresponding OAM spectrum for each mode was measured, as well as their approximated tip/tilt and displacement in the x and y directions. The experimentally measured OAM spectra and approximated tip/tilt and displacement values were used to generate a new testing dataset with input and output dimensions similar to the training dataset. The testing data comprises two sets of data: input data and output data. In the case of our network, the input is given by the transmitted mode, the approximated tip/tilt, and lateral displacement. At the same time, the output is their corresponding normalised power values of the OAM spectra. The experiment is performed with varying turbulence strengths corresponding to the following D/r_0 values: [0, 0.5, 0.7, 1, 1.1, 1.5, 2, 2.3, 2.7, 3] were used to generate the test dataset on input modes between $\ell_{\text{input}} = -5$ to 5. The generated test dataset had 18000 rows for the input and corresponding output values. The generated test dataset samples never participated in the neural network training process.

5.1.2 Experimental Verification of the Phase Screens

We simulated turbulence using Zernike polynomials, and the turbulence phase screens were first verified accordingly. The phase screens must be verified to ensure that their turbulence strength is consistent with the programmed value of D/r_0. The setup used to verify the simulated turbulence using Zernike polynomials is shown in Figure 5.2. SR value provides a convenient link between measured intensities and turbulence strength D/r_0. It is defined as the ratio of the average on-axis intensity with $\langle I(0)\rangle$ and without $I^0(0)$ turbulence. For a plane wave passing through a Gaussian lens in the Kolmogorov model, the following approximation can be used with excellent accuracy

$$\text{SR} = \frac{\langle I(0)\rangle}{I^0(0)} \approx \frac{1}{\left[1 + (D/r_0)^{5/3}\right]^{6/5}} \tag{5.7}$$

The procedure for verifying phase screens in the experiment is as follows: Various turbulence strengths are considered, typically ranging from $D/r_0 \in [0, 3]$. The SLM was used to create and display the turbulent screens, and for each turbulence strength, M (usually

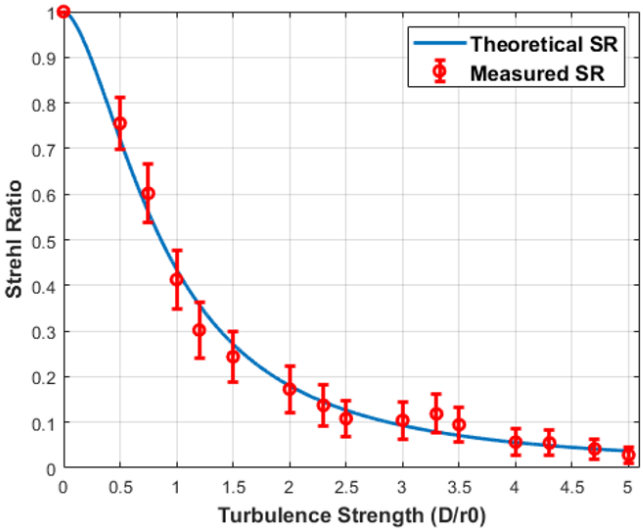

Figure 5.2: The Strehl ratio for a set of experimentally generated phase screens using the Zernike (Noll) methods. Theoretical values are plotted as solid lines, and experimentally measured points are represented as red dots superimposed with standard error bars. Experimental measurements of the Strehl Ratio show a close match to the theory.

100 or more worked well) turbulent screens were used. A Gaussian beam with a radius $w_0 = 0.35$ mm is directed onto the SLM, where D is related to w_0 by $D = \chi\, w_0$, with an initial value of χ set to $\sqrt{8}$ (about 2.83) [18]. The beam waist, the number of sub-harmonics and SLM screen resolution, among other factors, influence the turbulence strength experienced by the beams in the experiment. The χ value may require adjustment based on specific setup parameters to generate the screens. We measured the on-axis intensity for M screens, each representing a specific D/r_0 value, using a camera after passing the field through a lens to reach the far field. This process is repeated for the entire range of turbulence strengths. To normalise the measurements, we turn off the phase screens and measure the on-axis intensity in the absence of turbulence of the same Gaussian beam. The error in our measurements is calculated by dividing the standard deviation for M screens per D/r_0 value by $\sqrt{\text{M}}$. Comparing these measurements against the theoretical Strehl ratio in Equation (5.7) provides a single set of results. We aim to align the measured values with the theoretical ones, adjusting the factor χ relating the aperture D to the Gaussian beam waist. This adjustment produces a new turbulence strength, $\chi\, w_0/r_0$. We repeat this procedure for various χ values until achieving satisfactory agreement between the measured and theoretical Strehl ratio values. To improve the precision, we calculate the sum of the squares of the differences between theoretical and measured values. We then determine the optimal χ value through trial and error to minimise this sum. A $\chi = 2$ factor produced an excellent agreement between measured and theoretical values for numerical simulations and experimental measurements for screens generated with 250 orders of subharmonic terms. The plot depicted in Figure 5.2 shows results for the verified set of phase screens. The red markers with error bars represent the measured Strehl ratios, closely matching the programmed (theoretical) values indicated by the blue solid line.

5.1.3 Approximation of Tip/Tilt Zernike Terms

We verified the robustness of the approximation approach described in Chapter 3 in simulated turbulence. This was done to determine the SR values to generate the test dataset by approximating tip/tilt values from the Zernike terms in the presence and absence of the other higher-order Zernike terms. Based on the classical thin screen model, we leverage the

conclusions by Fried [86] and Noll [42] which showed that the tip/tilt occupies a majority of the energy contained in the turbulent distortions. In contrast, the other higher-order modes occupy much less. From the result of Noll, the 2nd (a_2) and the 3rd (a_3) Zernike coefficients are responsible for the tip/tilt, whereas the other high-order Zernike terms are responsible for the blur. As indicated by Equation (2) in [87], the relationship between the tip/tilt angles and the Zernike coefficient is given by

$$\begin{aligned} \text{tip} &= \frac{2\lambda}{\pi\omega_0} a_2 \\ \text{tilt} &= \frac{2\lambda}{\pi\omega_0} a_3 \end{aligned} \tag{5.8}$$

The procedure used to verify if the approximation method can be used to measure the tip/tilt from the Zernike terms was done in two steps as follows. Generate a Gaussian beam using the setup shown in Figure 5.1. Firstly, generate a phase screen using the 2nd and 3rd terms only and encode the Gaussian mode and the phase screen on the SLM as shown in Equation (5.6). The Gaussian is propagated to camera 1 to measure the tip/tilt angle approximations. For each phase screen, the randomly generated Zernike coefficients, a_j, for the 2nd and 3rd Zernike terms were known, and their corresponding tip/tilt angles of the 2nd and 3rd terms are calculated using Equation in [87].

The first measurements were made by calculating the tip/tilt angles of the 2nd and 3rd Zernike terms, which are then compared with their corresponding tip/tilt approximations. The same steps were followed for the second measurement except that the phase screens were generated using the 2nd, 3rd, and higher-order Zernike terms. Using only the 2nd and 3rd Zernike coefficients in the presence of the higher-order Zernike terms, the tip/tilt angles were calculated using Equation in (5.8) and their corresponding tip/tilt angle approximations were made using camera 1. Similarly, the computed tip/tilt angles of the 2nd and 3rd Zernike terms are then compared with the corresponding tip/tilt approximations, and two observations were of interest. The first observation was how well the approximation method can estimate the tip/tilt angles from the 2nd and 3rd Zernike terms. The second observation was on the effect of the higher-order terms on the estimation of the tip/tilt angles from the 2nd and 3rd Zernike.

Turbulence strength was increased from D/r_0 is 0 to 3, and the calculated tip/tilt values were still within the training range; the results are shown in Figure 5.3. Figure 5.3(a) shows the line-of-best fit in the presence of higher-order moves away from the line-of-best fit of tip/tilt only as the strength turbulence increases. The line-of-best fit of the tip/tilt approximation remains relatively the same despite the increase in turbulence strength. The higher-order Zernike terms distort the beam's intensity profile (and phase) as shown in Figure 5.3(b), and their effect increases as turbulence strength is increased. Therefore, the approximation approach can be used to estimate tip/tilt using Zernike terms. The tip/tilt estimation accuracy drops in the presence of higher-order terms because the approximation approach uses the beam's intensity distribution. Unfortunately, it is difficult to determine the displacement values in the absence and presence of higher-order Zernike terms. The approximation approach for displacement measurements was still assumed to suffice. This approximation approach can estimate tip/tilt and displacement in the presence of higher-order Zernike terms to use as input for the NN models. However, the effect of the higher-order terms on the model's ability to model OAM crosstalk is yet to be seen.

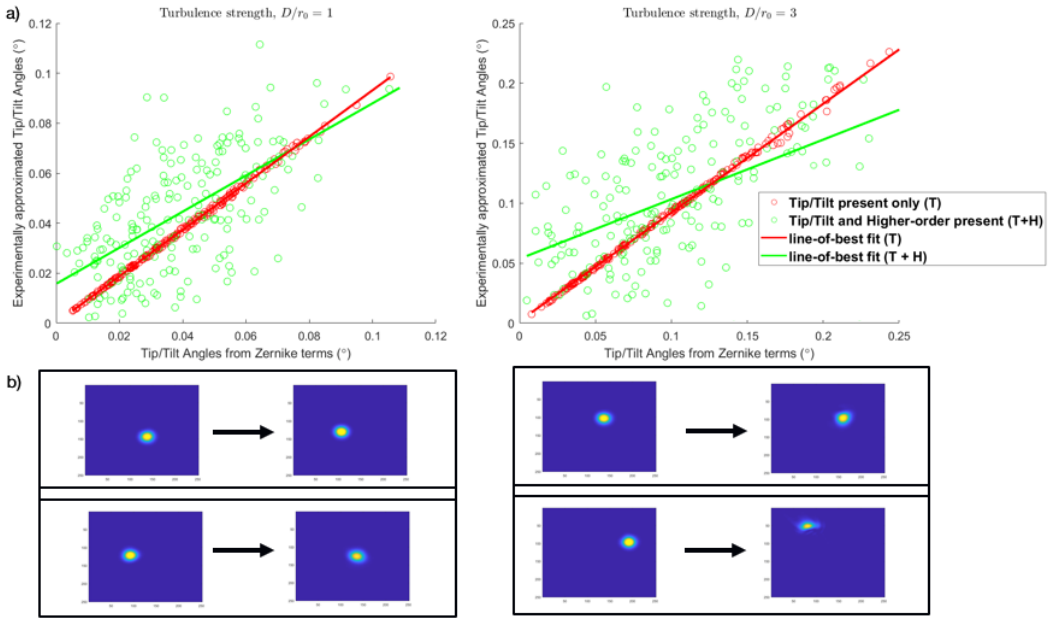

Figure 5.3: Experimental validation of Zernike tip/tilt terms, illustrated by (a) the presence (green dots) and absence (red dots) of higher-order Zernike terms under turbulence strengths, $D/r_0 = 1$ and 3. (b) Random images of the Gaussian beam under turbulence strengths, $D/r_0 = 1$ and 3, demonstrating the evolving profile and distribution with the introduction of tip/tilt terms alone and in combination with higher-order terms.

5.2 Results and Discussion

5.2.1 Comparison of NN-estimation with Measured Turbulent OAM Spectra

In this section, we test the ability of our previously trained NN model to estimate OAM spectra under turbulent conditions without the need for retraining. The model, initially trained on known tip/tilt and displacement values in Chapter 4, now applies this training to estimate OAM spectra under simulated turbulence conditions using the approximated tip/tilt and displacement values without the need for retraining. Figures 5.4, 5.5, and 5.6 present an analysis of our results.

Figure 5.4 illustrates the NN-estimated OAM spectra without retraining (in green) compared to the experimentally measured spectra under simulated turbulence (in red). We observed a close match between the two spectra across various turbulence strengths, as indicated by the low RMSE values. The coefficient of determination values depicted in Figure 5.5 provide insight into the model's performance. We found a coefficient of determination of 0.88 for the NN-estimated OAM spectra under turbulence, compared to 0.91 for the spectra estimated using known tip/tilt and displacement values. This suggests the model performs slightly better with known inputs but still provides accurate estimations under turbulent conditions without retraining.

Figure 5.6 shows the residual plot of the NN-estimated OAM spectra, highlighting the RMSE values across different turbulence strengths. The RMSE ranges from 0.01 to 0.11 with a mean value of 0.07, where the more significant approximated tip/tilt and displacement values correspond to a larger RMSE. The RMSE of the NN estimated spectra increases as the turbulence strength increases. This is because the variance of both the tip/tilt orders and the higher orders increases with the turbulence strength, causing an increase in the RMSE value. The rise in RMSE with turbulence strength can be attributed to the variance of both

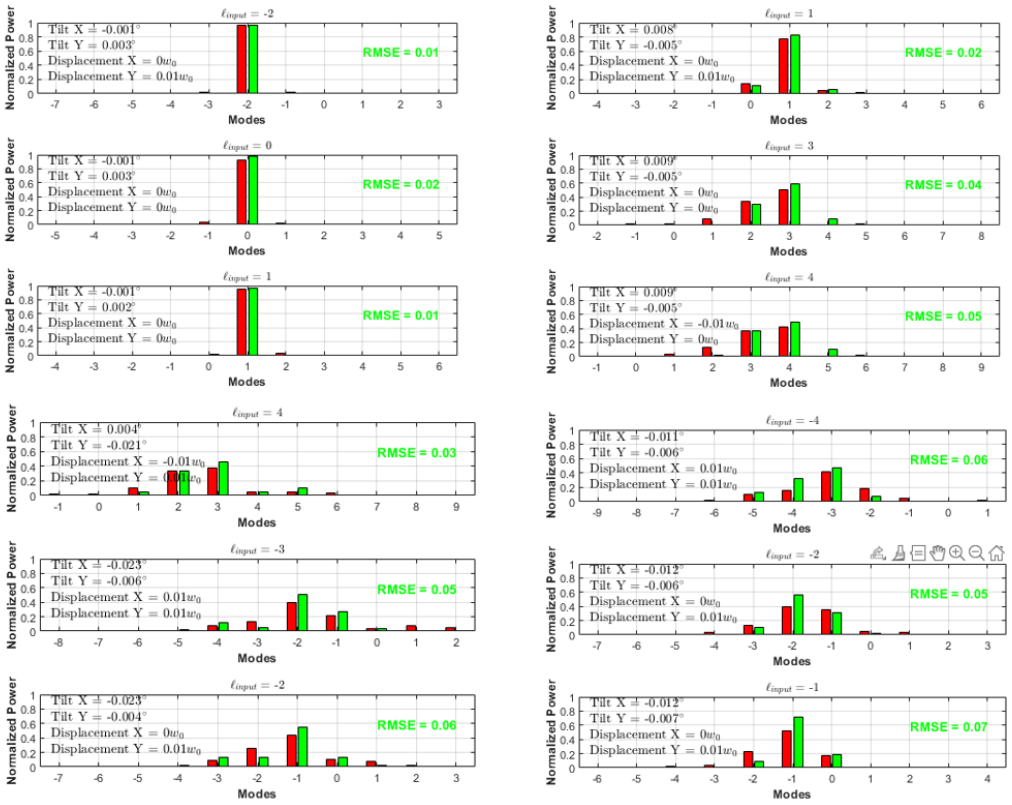

Figure 5.4: In the presence of turbulence, we can still estimate the tip/tilt and displacement. The approximated tip/tilt and displacement values and their corresponding OAM spectra of random input modes, $\ell_{\text{input}} \in$ [-5,5], were used to generate the unseen dataset to test the NN model without retraining the model. The bar plots above show the NN-estimated OAM spectra without retraining (in green) and measured spectra due to simulated turbulence (in red). The RMSE between the two spectra is shown in each plot.

tip/tilt orders and higher orders, which magnify with increased turbulence. Additionally, the impact of other turbulence effects, beyond tip/tilt terms, contributes to a minor decrease in the coefficient of determination by less than 5%.

Our findings match with previous studies [18], indicating that tip/tilt terms dominate atmospheric turbulence effects due to their more significant coefficients. However, it is essential to acknowledge the limitations of our study. Although the overall NN estimations of the OAM spectra are a good fit in the presence of turbulence, the values of the approximated displacement in the simulated turbulence are small in magnitude across the turbulence strengths, showing that the model's estimations are pre-dominant due to the tip/tilt contributions than the displacement. Therefore, the trained model can accurately estimate the OAM crosstalk in the presence of turbulence. Future studies could explore methods to improve the model's performance under these conditions.

5.3 Conclusion

Tip/tilt terms dominate atmospheric turbulence, comprising 86% of the mean-square phase value. We experimentally generated and verified the testing dataset of approximated inputs in the thin phase, Kolmogorov regime, across various turbulence strengths. Our simple neural network, trained exclusively on tip/tilt and displacement inputs without retraining,

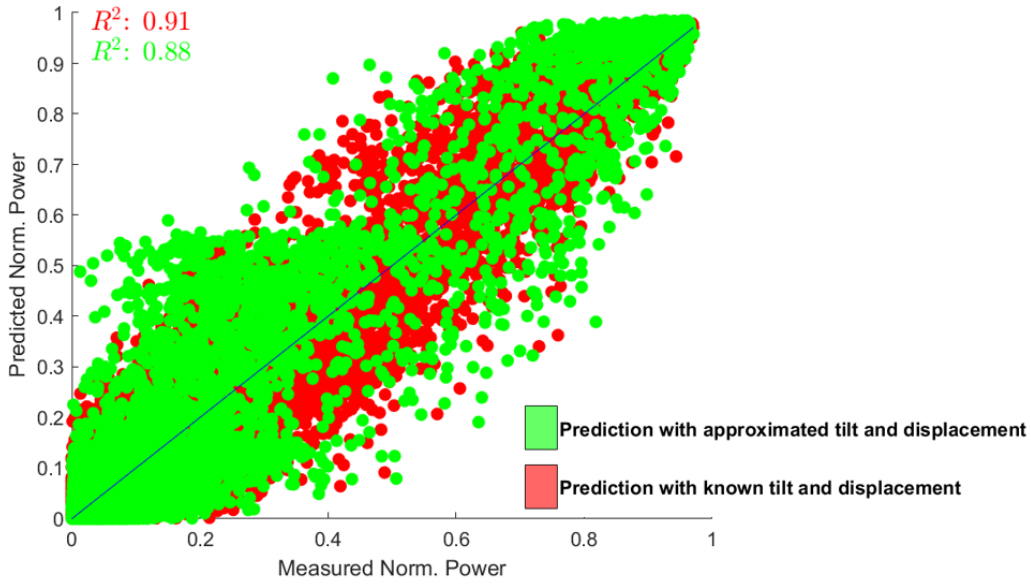

Figure 5.5: The correlation plot shows a comparison between NN-estimated OAM spectra and experimentally measured spectra for the measurements approximated in the presence of turbulence (in green) and the known tip/tilt and displacement measured in Chapter 3 (in red). The coefficient of determination for the measurements with tip/tilt and displacement (in green) and in the presence of turbulence (in red).

accurately estimated OAM spectra using approximated input values in turbulent aberrations. The model's coefficient of determination shows only a minimal drop in the presence of turbulence aberration, showing that a simple neural network produces good results in the presence of the other multitude of turbulence aberrations. This is significant because a simple detector like a camera or photodiode can help digital signal processing and error correction coding techniques to detect and correct errors caused by crosstalk for improved MDM performance.

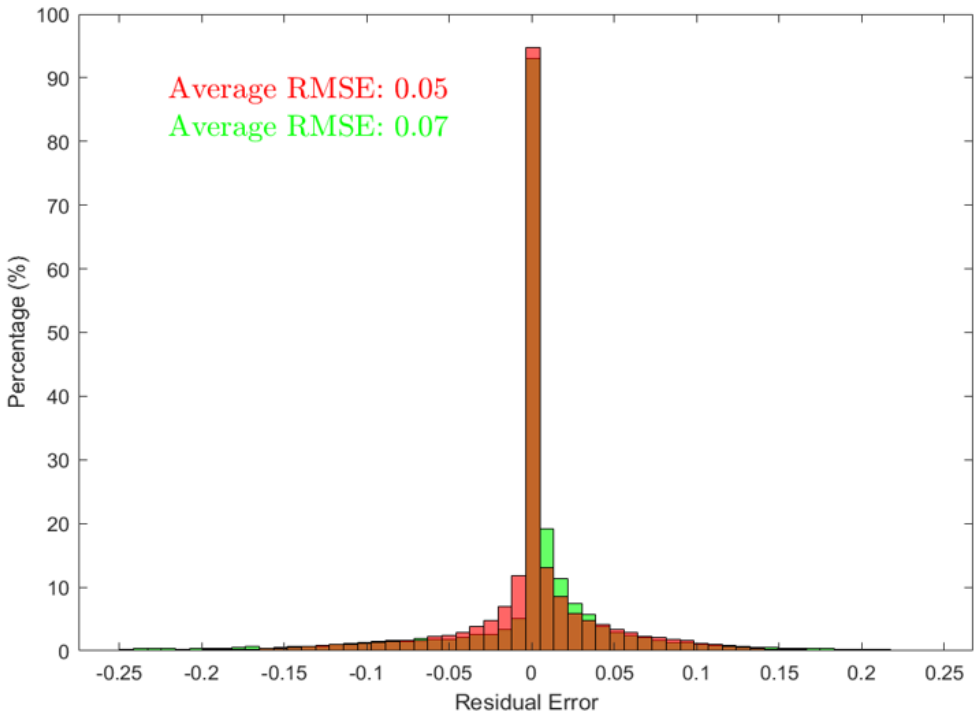

Figure 5.6: Residual plots showing the average RMSE for the measurements with tip/tilt and displacement (in green) and in the presence of turbulence (in red). The histogram of the residuals exhibits a random Gaussian characteristic shape.

CHAPTER 6

Conclusion

THIS research addresses the challenge of extending the range of FSO links, particularly MDM systems using OAM beams. While FSO-MDM has shown promise over short distances, extending this range to kilometres is hindered by severe atmospheric turbulence-induced crosstalk, degrading system performance. The limited spatial subchannels due to receiver size and beam expansion pose challenges for long-distance MDM systems. This research addressed the challenge of atmospheric turbulence in extending the range of FSO-MDM systems - OAM crosstalk due to turbulence. The primary aim was to develop a simple neural network model to estimate OAM crosstalk induced by atmospheric turbulence effects such as lateral displacement and tip/tilt. Results of the development and testing of the same model have been presented.

The main research question that this work is answering is "*How can neural networks be used to model OAM crosstalk in FSO systems using OAM modes, particularly in the presence of atmospheric turbulence-induced aberrations such as lateral displacement, tip/tilt, and other aberrations of turbulence?*".

Due to the lack of an open-source dataset of tip/tilt, displacement, and OAM crosstalk, a dataset had to be generated to train the neural network. Chapter 3 presents a comprehensive approach to characterising OAM crosstalk due to tip/tilt and displacement, detailing experimental setups, dataset generation, simulation validation, and measurement verification. The results show a strong correlation between measured and simulated OAM spectra, providing confidence in the training dataset for the neural network model development in Chapter 4.

In Chapter 4, the development of the model architecture and its training process is outlined. The results showed a simple neural network model trained with the specified parameters, which achieved a small worst-case absolute error of normalised power on the validation set. The high correlation coefficient also indicates a strong match between estimated and simulated OAM crosstalk used as targets for the case with a combination of tilt and displacement. These metrics demonstrate the model's capability to accurately estimate OAM crosstalk under lateral displacement and tip/tilt on different combinations. The model estimates the OAM crosstalk accurately in the case of a combination of tip/tilt and displacement.

In Chapter 5, the experimental setup used to generate the testing dataset is described, including the simulation of turbulence using Zernike polynomials. The neural network model, initially trained with lateral displacement and tip/tilt on OAM modes in Chapter 4, was tested for its ability to estimate OAM crosstalk under the presence of additional turbulence aberrations beyond tip/tilt and displacement without retraining. Across various

turbulence strengths, the NN-estimated OAM spectra closely match the experimentally measured spectra with low Root Mean Square Error (RMSE) values. Comparing the model's performance on known inputs (tip/tilt and displacement only) and approximated inputs in the presence of turbulence shows that the simple model had highly accurate estimations, with the coefficient of determinations having a minimal decrease. This indicates the model can generalise the OAM estimations using approximated measurements in the presence of additional aberrations without retraining.

Our findings indicate that a simple neural network trained solely on tilt and displacement can give good results in the presence of the other multitude of turbulence aberrations. This is significant because it means a simple detector like a camera or quadrant photodiode can help digital signal processing to detect and correct errors caused by crosstalk. This research contributes valuable insights into modelling OAM crosstalk in FSO systems using neural networks, particularly in turbulent environments. The results suggest that a simple neural network can effectively estimate OAM crosstalk induced by atmospheric turbulence aberrations, offering a proof-of-concept for models that can be used to implement or optimise techniques to mitigate crosstalk errors in MDM systems.

6.1 Future Work

The work presented here addresses fundamental questions that can improve the performance of FSO communication systems, especially for long-distance applications. This research has shown how a simple neural network can accurately model OAM crosstalk, particularly in atmospheric turbulence-induced effects like tip/tilt and displacement. These findings suggest that neural networks can potentially enhance the reliability and efficiency of long-distance MDM systems in challenging atmospheric conditions.

The next phase of this research could involve expanding the current neural network model to include other architectures like recurrent neural networks or models with long short-term memory. These models can learn from sequential data, essential because turbulence-induced changes in optical signal intensity are correlated over time, typically spanning several milliseconds. Similarly, there are temporal correlations between OAM crosstalk spectra due to turbulence [43].

By incorporating a memory model, we might gain insights into forecasting future OAM crosstalk and even develop a model for how OAM crosstalk evolves. Given the temporal correlation between OAM crosstalk spectra, we can explore ways to estimate future crosstalk based on past and present information from devices such as a camera [43]. MIMO DSP has been shown to help mitigate the effects of atmospheric turbulence in the MDM FSO systems [88]. By incorporating knowledge of future crosstalk into MIMO DSP algorithms, the system can proactively adjust signal processing to mitigate anticipated crosstalk. This information informs critical design parameters in a communication system, such as frame length, inter-leaver depth and error correction code length. Such predictive capabilities could lead to more effective MDM or modal diversity systems signal-processing strategies. Therefore, increasing the quality of the signal detected at the receiver ultimately improves the performance and the quality of service of MDM systems in turbulent conditions.

References

[1] M. A. Khalighi and M. Uysal, "Survey on free space optical communication: A communication theory perspective," *IEEE Communications Surveys and Tutorials*, vol. 16, no. 4, pp. 2231–2258, Apr. 2014.

[2] P. J. Winzer and R. J. Essiambre, "Advanced optical modulation formats," *Proceedings of the IEEE*, vol. 94, no. 5, pp. 952–981, 2006.

[3] B. Mukherjee, "WDM optical communication networks: Progress and challenges," *IEEE Journal on Selected Areas in Communications*, vol. 18, no. 10, pp. 1810–1824, Oct. 2000.

[4] E. Ciaramella *et al.*, "1.28-Tb/s (32 × 40 Gb/s) Free-Space Optical WDM Transmission System," *IEEE Photonics Technology Letters*, vol. 21, no. 16, pp. 1121–1123, Aug. 2009.

[5] D. J. Richardson, J. M. Fini, and L. E. Nelson, "Space-division multiplexing in optical fibres," *Nature Photonics 2013 7:5*, vol. 7, no. 5, pp. 354–362, Apr. 2013.

[6] G. Gibson *et al.*, "Free-space information transfer using light beams carrying orbital angular momentum," *Optics Express, Vol. 12, Issue 22, pp. 5448-5456*, vol. 12, no. 22, pp. 5448–5456, Nov. 2004.

[7] J. Wang *et al.*, "Terabit free-space data transmission employing orbital angular momentum multiplexing," *Nature Photonics 2012 6:7*, vol. 6, no. 7, pp. 488–496, Jun. 2012.

[8] J. Wang, J. Liu, S. Li, Y. Zhao, J. Du, and L. Zhu, "Orbital angular momentum and beyond in free-space optical communications," *Nanophotonics*, vol. 11, no. 4, pp. 645–680, Jan. 2022.

[9] Y. Yan *et al.*, "High-capacity millimetre-wave communications with orbital angular momentum multiplexing," *Nature Communications 2014 5:1*, vol. 5, no. 1, pp. 1–9, Sep. 2014.

[10] Z. Zhao *et al.*, "Optical communications using orbital angular momentum beams," *Advances in Optics and Photonics, Vol. 7, Issue 1, pp. 66-106*, vol. 7, no. 1, pp. 66–106, Mar. 2015.

[11] L. Allen, M. W. Beijersbergen, R. J. Spreeuw, and J. P. Woerdman, "Orbital angular momentum of light and the transformation of Laguerre-Gaussian laser modes," *Physical Review A*, vol. 45, no. 11, p. 8185, Jun. 1992.

[12] A. Mair, A. Vaziri, G. Weihs, and A. Zeilinger, "Entanglement of the orbital angular momentum states of photons," *Nature 2001 412:6844*, vol. 412, no. 6844, pp. 313–316, Jul. 2001.

[13] A. M. Yao and M. J. Padgett, "Orbital angular momentum: origins, behavior and applications," *Advances in Optics and Photonics, Vol. 3, Issue 2, pp. 161-204*, vol. 3, no. 2, pp. 161–204, Jun. 2011.

[14] S. M. Barnett and L. Allen, "Orbital angular momentum and nonparaxial light beams," *Optics Communications*, vol. 110, no. 5-6, pp. 670–678, Sep. 1994.

[15] H. Huang *et al.*, "100 Tbit/s free-space data link enabled by three-dimensional multiplexing of orbital angular momentum, polarization, and wavelength," *Optics Letters, Vol. 39, Issue 2, pp. 197-200*, vol. 39, no. 2, pp. 197–200, Jan. 2014.

[16] J. Wang *et al.*, "N-dimentional multiplexing link with 1.036-Pbit/s transmission capacity and 112.6-bit/s/Hz spectral efficiency using OFDM-8QAM signals over 368 WDM pol-muxed 26 OAM modes," *European Conference on Optical Communication, ECOC*, Nov. 2014.

[17] V. W. Chan, "Free-space optical communications," *Journal of Lightwave Technology*, vol. 24, no. 12, pp. 4750–4762, 2006.

[18] L. C. Andrews and R. L. Phillips, "Laser beam propagation through random media: Second edition," *Laser Beam Propagation Through Random Media: Second Edition*, pp. 1–783, Sep. 2005.

[19] L. C. Andrews, R. L. Phillips, and A. R. Weeks, "Propagation of a Gaussian-beam wave through a random phase screen," *Waves in Random Media*, vol. 7, no. 2, pp. 229–244, 1997.

[20] Y. Ren *et al.*, "Atmospheric turbulence effects on the performance of a free space optical link employing orbital angular momentum multiplexing," *Optics Letters*, vol. 38, no. 20, p. 4062, Oct. 2013.

[21] C. Paterson, "Atmospheric Turbulence and Orbital Angular Momentum of Single Photons for Optical Communication," 2005.

[22] G. A. Tyler and R. W. Boyd, "Influence of atmospheric turbulence on the propagation of quantum states of light carrying orbital angular momentum," Tech. Rep. 2, 2009.

[23] J. A. Anguita, M. A. Neifeld, and B. V. Vasic, "Turbulence-induced channel crosstalk in an orbital angular momentum-multiplexed free-space optical link," *Applied Optics*, vol. 47, no. 13, pp. 2414–2429, May 2008.

[24] A. E. Willner, K. Pang, H. Song, K. Zou, and H. Zhou, *Orbital angular momentum of light for communications*, Dec. 2021.

[25] P. Liao *et al.*, "Experimental characterization of a 400Gbit/s orbital angular momentum multiplexed free-space optical link over 120 m," *Optics Letters, Vol. 41, Issue 3, pp. 622-625*, vol. 41, no. 3, pp. 622–625, Feb. 2016.

[26] Z. Qu and I. B. Djordjevic, "500Gb/s free-space optical transmission over strong atmospheric turbulence channels," *Optics Letters, Vol. 41, Issue 14, pp. 3285-3288*, vol. 41, no. 14, pp. 3285–3288, Jul. 2016.

[27] Y. Ren *et al.*, "Orbital Angular Momentum-based Space Division Multiplexing for High-capacity Underwater Optical Communications," *Nature Publishing Group*, 2016.

[28] L. Li *et al.*, "High-Capacity Free-Space Optical Communications between a Ground Transmitter and a Ground Receiver via a UAV Using Multiplexing of Multiple Orbital-Angular-Momentum Beams," *Scientific Reports*, vol. 7, no. 1, Dec. 2017.

[29] Y. Li, M. Patel, A. Ali, Z. Hu, D. M. Benton, and A. D. Ellis, "Demonstration of 10-channel mode- and polarization-division multiplexed free-space optical transmission with successive interference cancellation DSP," *Optics Letters, Vol. 47, Issue 11, pp. 2742-2745*, vol. 47, no. 11, pp. 2742–2745, Jun. 2022.

[30] M. Tur *et al.*, "400-Gbit/s QPSK free-space optical communication link based on four-fold multiplexing of Hermite Gaussian or Laguerre Gaussian modes by varying both modal indices," *Optics Letters, Vol. 43, Issue 16, pp. 3889-3892*, vol. 43, no. 16, pp. 3889–3892, Aug. 2018.

[31] M. Krenn *et al.*, "Twisted light transmission over 143 km," *Proceedings of the National Academy of Sciences of the United States of America*, vol. 113, no. 48, pp. 13 648–13 653, Nov. 2016.

[32] Y. Awaji, N. Wada, and Y. Toda, "Demonstration of spatial mode division multiplexing using Laguerre-Gaussian mode beam in telecom-wavelength," *2010 23rd Annual Meeting of the IEEE Photonics Society, Photonics 2010*, pp. 551–552, 2010.

[33] P. Martelli, A. Gatto, P. Boffi, and M. Martinelli, "Free-space optical transmission with orbital angular momentum division multiplexing," *Electronics Letters*, vol. 47, no. 17, pp. 972–973, Aug. 2011.

[34] J. Wang *et al.*, "Demonstration of 12.8-bit/s/Hz Spectral Efficiency using 16-QAM Signals over Multiple Orbital-Angular-Momentum Modes," *37th European Conference and Exposition on Optical Communications (2011), paper We.10.P1.76*, We.10.P1.76, Sep. 2011.

[35] Z. Zheng, Y. Zhu, F. Zhang, and K. Zou, "1λ & 1.44 Tb/s free-space IM-DD transmission employing OAM multiplexing and PDM," *Optics Express, Vol. 24, Issue 4, pp. 3967-3980*, vol. 24, no. 4, pp. 3967–3980, Feb. 2016.

[36] F. E. Mahmouli and S. D. Walker, "4-gbps uncompressed video transmission over a 60-GHz orbital angular momentum wireless channel," *IEEE Wireless Communications Letters*, vol. 2, no. 2, pp. 223–226, 2013.

[37] Z. Hu *et al.*, "Aiming for high-capacity multi-modal free-space optical transmission leveraging complete modal basis sets," *Optics Communications*, vol. 541, p. 129 531, 2023.

[38] Yifan Zhao *et al.*, "Experimental Demonstration of 260-meter Security Free-Space Optical Data Transmission Using 16-QAM Carrying Orbital Angular Momentum (OAM) Beams Multiplexing," *2016 Optical Fiber Communication Conference*, vol. 16, no. 1931-9401, p. 041 312, Oct. 2016.

[39] H. Hemmati, *Near-Earth Laser Communications*, CRC Press. 2020, pp. 1–40.

[40] J. Lin, X.-C. Yuan, M. Chen, and J. C. Dainty, "Application of orbital angular momentum to simultaneous determination of tilt and lateral displacement of a misaligned laser beam," *J. Opt. Soc. Am. A*, vol. 27, pp. 2337–2343, 2010.

[41] M. V. Vasnetsov, V. A. Pas'ko, and M. S. Soskin, "Analysis of orbital angular momentum of a misaligned optical beam," *New Journal of Physics*, vol. 7, Feb. 2005.

[42] R. J. Noll, "Zernike Polynomials and Atmospheric Turbulence.," *J Opt Soc Am*, vol. 66, no. 3, pp. 207–211, 1976.

[43] M. A. Cox, L. Gailele, L. Cheng, and A. Forbes, "Modelling the Memory of Turbulence-Induced Beam Wander," *arXiv preprint arXiv:1907.10519*, vol. 1, Jul. 2019.

[44] A. Forbes, B. Sephton, I. Nape, J. Pinnell, M. A. Cox, and V. Rodríguez-Fajardo, "Modal analysis of structured light with spatial light modulators: a practical tutorial," *JOSA A, Vol. 37, Issue 11, pp. C146-C160*, vol. 37, no. 11, pp. C146–C160, Nov. 2020.

[45] A. E. Willner *et al.*, *Recent advances in high-capacity free-space optical and radio-frequency communications using orbital angular momentum multiplexing*, Feb. 2017.

[46] F. Roddier, "The Effects of Atmospheric Turbulence in Optical Astronomy," *Progress in Optics*, vol. 19, no. C, pp. 281–376, Jan. 1981.

[47] D. Bachmann, M. Isoard, V. Shatokhin, G. Sorelli, and A. Buchleitner, "Accurate Zernike-Corrected Phase Screens for Arbitrary Power Spectra," 2024.

[48] X. Zhu and J. M. Kahn, "Free-Space Optical Communication Through Atmospheric Turbulence Channels," *IEEE TRANSACTIONS ON COMMUNICATIONS*, vol. 50, no. 8, p. 1293, 2002.

[49] M. A. Cox, N. Mphuthi, I. Nape, N. Mashaba, L. Cheng, and A. Forbes, "Structured Light in Turbulence," *IEEE Journal of Selected Topics in Quantum Electronics*, vol. 27, no. 2, pp. 1–21, Sep. 2020.

[50] F. Dios, J. A. Rubio, A. Rodríguez, and A. Comerón, "Scintillation and beam-wander analysis in an optical ground station-satellite uplink," *Applied Optics, Vol. 43, Issue 19, pp. 3866-3873*, vol. 43, no. 19, pp. 3866–3873, Jul. 2004.

[51] A. Rodriguez-Gomez, F. Dios, J. A. Rubio, and A. Comeron, "Temporal statistics of the beam-wander contribution to scintillation in ground-to-satellite optical links: an analytical approach," *Applied Optics, Vol. 44, Issue 21, pp. 4574-4581*, vol. 44, no. 21, pp. 4574–4581, Jul. 2005.

[52] D. H. Tofsted, "Outer-scale effects on beam-wander and angle-of-arrival variances," *Applied Optics, Vol. 31, Issue 27, pp. 5865-5870*, vol. 31, no. 27, pp. 5865–5870, Sep. 1992.

[53] J. A. Anguita, M. A. Neifeld, and B. V. Vasic, "Modeling channel interference in an orbital angular momentum-multiplexed laser link," in *Free-Space Laser Communications IX*, vol. 7464, SPIE, Aug. 2009, 74640U.

[54] B. Rodenburg *et al.*, "Influence of atmospheric turbulence on states of light carrying orbital angular momentum," Tech. Rep., 2012.

[55] M. A. Cox, L. Maqondo, R. Kara, G. Milione, L. Cheng, and A. Forbes, "The Resilience of Hermite-and Laguerre-Gaussian Modes in Turbulence," *Journal of Lightwave Technology*, vol. 37, no. 16, pp. 3911–3917, 2019.

[56] G. Xie *et al.*, "Performance metrics and design considerations for a free-space optical orbital-angular-momentum–multiplexed communication link," *Optica*, vol. 2, no. 4, p. 357, Apr. 2015.

[57] A. Klug, I. Nape, and A. Forbes, "The orbital angular momentum of a turbulent atmosphere and its impact on propagating structured light fields," *New Journal of Physics*, vol. 23, no. 9, p. 093 012, Sep. 2021.

[58] M. P. Lavery *et al.*, "Free-space propagation of high-dimensional structured optical fields in an urban environment," *Science Advances*, vol. 3, no. 10, 2017.

[59] S. Sharma, S. Sharma, and A. Athaiya, "Activation Function in Neural Networks," *International Journal of Engineering Applied Sciences and Technology*, vol. 4, pp. 310–316, 2020.

[60] J. I. Janjua, S. Zulfiqar, T. A. Khan, and S. A. Ramay, "Activation Function Conundrums in the Modern Machine Learning Paradigm," in *ICCA 2023 - 2023 5th International Conference on Computer and Applications, Proceedings*, Institute of Electrical and Electronics Engineers Inc., 2023.

[61] H. Borchani, G. Varando, C. Bielza, and P. Larrañaga, "A survey on multi-output regression," *Wiley Interdisciplinary Reviews: Data Mining and Knowledge Discovery*, vol. 5, no. 5, pp. 216–233, Sep. 2015.

[62] Y. Lecun, Y. Bengio, and G. Hinton, "Deep learning," *Nature*, vol. 521, no. 7553, pp. 436–444, May 2015.

[63] I. Goodfellow, Y. Bengio, and A. Courville, *Deep Learning*. MIT Press, 2016, vol. 1.

[64] C. C. Aggarwal, *Neural Networks and Deep Learning*. Springer International Publishing, 2018.

[65] A. D. Rasamoelina, F. Adjailia, and P. Sincak, "A Review of Activation Function for Artificial Neural Network," *SAMI 2020 - IEEE 18th World Symposium on Applied Machine Intelligence and Informatics, Proceedings*, pp. 281–286, Jan. 2020.

[66] S. Hikmat Haji and A. Mohsin Abdulazeez, "Comparison Of Optimization Techniques Based On Gradient Descent Algorithm: A Review," *Journal Of Archaeology Of Egypt/Egyptology*, vol. 18, no. 4, pp. 2715–2743,

[67] J. Chu, D. Chu, and Q. Smithwitck, "Off-axis points encoding/decoding with orbital angular momentum spectrum," *Scientific Reports 2017 7:1*, vol. 7, no. 1, pp. 1–9, Mar. 2017.

[68] M. Elamassie, H. Tadayyoni, and M. Uysal, "Characterization of Orbital Angular Momentum-Multiplexed FSO Channel in the Presence of Pointing Errors," *31st IEEE Conference on Signal Processing and Communications Applications, SIU 2023*, 2023.

[69] P. Zhao *et al.*, "Identifying the tilt angle and correcting the orbital angular momentum spectrum dispersion of misaligned light beam," *Scientific Reports*, vol. 7, no. 1, pp. 1–10, 2017.

[70] Y. Ding *et al.*, "Analysis of misaligned optical rotational Doppler effect by modal decomposition," *Optics Express*, vol. 29, no. 10, p. 15 288, 2021.

[71] R. Singh, J. M. Hattuniemi, and A. J. Mäkynen, "Analysis of accuracy of laser spot centroid estimation," in *Advanced Laser Technologies 2007*, vol. 7022, SPIE, Jun. 2008, pp. 354–359.

[72] Z. Jiang, S. Gong, and Y. Dai, "Monte-Carlo analysis of centroid detected accuracy for wavefront sensor," *Optics & Laser Technology*, vol. 37, pp. 541–546, 2005.

[73] P. Schober and L. A. Schwarte, "Correlation coefficients: Appropriate use and interpretation," *Anesthesia and Analgesia*, vol. 126, no. 5, pp. 1763–1768, May 2018.

[74] D. Zia *et al.*, "Regression of high dimensional angular momentum states of light," *Physical Review Research*, vol. 5, no. 1, Jun. 2022.

[75] B. Pinheiro Da Silva, B. A. D. Marques, R. B. Rodrigues, ‡. P. H. Souto Ribeiro, and A. Z. Khoury, "Machine learning recognition of light orbital-angular-momentum superpositions," *Phys. Rev. A*, 2020.

[76] X. Yuan *et al.*, "Dual-Output Mode Analysis of Multimode Laguerre-Gaussian Beams via Deep Learning," *Optics 2021, Vol. 2, Pages 87-95*, vol. 2, no. 2, pp. 87–95, May 2021.

[77] G. Jing *et al.*, "Recognizing fractional orbital angular momentum using feed forward neural network," *Physics*, vol. 28, p. 104 619, 2021.

[78] Y. He *et al.*, "Detecting Orbital Angular Momentum Modes of Vortex Beams Using Feed-Forward Neural Network," *Journal of Lightwave Technology*, vol. 37, no. 23, pp. 5848–5855, Dec. 2019.

[79] D. Briantcev, M. A. Cox, M. A. Cox, A. Trichili, B. S. Ooi, and M.-S. Alouini, "Beam wander prediction with recurrent neural networks," *Optics Express, Vol. 31, Issue 18, pp. 28859-28873*, vol. 31, no. 18, pp. 28 859–28 873, Aug. 2023.

[80] D. Chicco, M. J. Warrens, and G. Jurman, "The coefficient of determination R-squared is more informative than SMAPE, MAE, MAPE, MSE and RMSE in regression analysis evaluation," *PeerJ Comput Sci*, vol. 7, Aug. 2021.

[81] A. Trichili, M. A. Cox, B. S. Ooi, and M.-S. Alouini, "Roadmap to free space optics," *Journal of the Optical Society of America B*, vol. 37, no. 11, A184, Nov. 2020.

[82] Y. Li, M. Chen, Y. Yang, M. T. Zhou, and C. Wang, "Convolutional recurrent neural network-based channel equalization: An experimental study," *2017 23rd Asia-Pacific Conference on Communications: Bridging the Metropolitan and the Remote, APCC 2017*, vol. 2018-January, pp. 1–6, Jul. 2017.

[83] A. C. Motlagh, V. Ahmadi, Z. Ghassemlooy, and K. Abedi, "The effect of atmospheric turbulence on the performance of the free space optical communications," *Proceedings of the 6th International Symposium Communication Systems, Networks and Digital Signal Processing, CSNDSP 08*, pp. 540–543, 2008.

[84] Y. Wu, A. Wang, and L. Zhu, "Direct prediction and compensation of atmospheric turbulence for free-space integer and fractional order OAM multiplexed transmission links," *Optics Express*, vol. 31, no. 22, p. 36 078, Oct. 2023.

[85] D. E. Silva and J. Y. Wang, "Wave-front interpretation with Zernike polynomials," *Applied Optics, Vol. 19, Issue 9, pp. 1510-1518*, vol. 19, no. 9, pp. 1510–1518, May 1980.

[86] D. L. Fried, "Statistics of a Geometric Representation of Wavefront Distortion," *JOSA, Vol. 55, Issue 11, pp. 1427-1435*, vol. 55, no. 11, pp. 1427–1435, Nov. 1965.

[87] G. A. Chanan, "Calculation of wave-front tilt correlations associated with atmospheric turbulence," *JOSA A, Vol. 9, Issue 2, pp. 298-301*, vol. 9, no. 2, pp. 298–301, Feb. 1992.

[88] G. Xie *et al.*, "Crosstalk mitigation in a free-space orbital angular momentum multiplexed communication link using 4×4 MIMO equalization," *Optics Letters, Vol. 39, Issue 15, pp. 4360-4363*, vol. 39, no. 15, pp. 4360–4363, Aug. 2014.